Synoptic View of the North Atlantic Oscillation

JAMES J. BENEDICT* AND SUKYOUNG LEE

Department of Meteorology, The Pennsylvania State University, University Park, Pennsylvania

STEVEN B. FELDSTEIN

EMS Environment Institute, The Pennsylvania State University, University Park, Pennsylvania

(Manuscript received 4 December 2002, in final form 1 August 2003)

ABSTRACT

This article investigates the synoptic characteristics of individual North Atlantic Oscillation (NAO) events by examining the daily evolution of the potential temperature field on the nominal tropopause (the 2-PVU surface). This quantity is obtained from the National Centers for Environmental Prediction–National Center for Atmospheric Research (NCEP–NCAR) reanalysis dataset for the winter season.

For both phases, the NAO is found to originate from synoptic-scale waves. As these waves evolve into the low-frequency NAO pattern, they break anticyclonically for the positive phase and cyclonically for the negative phase. The results of this analysis suggest that it is the remnants of these breaking waves that form the physical entity of the NAO. Throughout the NAO events, for both phases, the NAO is maintained by the successive breaking of upstream synoptic-scale waves. When synoptic-scale disturbances are no longer present, mixing processes play an important role in the NAO decay. As in other recent studies of the NAO, it is found that these individual NAO events complete their life cycle in a time period of about two weeks.

Additional differences between the wave breaking characteristics of the two NAO phases are found. For the positive NAO phase, anticyclonic wave breaking takes place in two regions: one over the North Atlantic and the other near the North American west coast. For the negative NAO phase, on the other hand, there is a single breaking wave confined to the North Atlantic. An explanation based on kinematics is given to account for this difference.

1. Introduction

The North Atlantic Oscillation (NAO), one of the most dominant teleconnection patterns in the atmosphere, has recently received much attention, as it has been suggested that the NAO is not only related to European weather and climate but also to the hemispheric-scale circulation (Thompson and Wallace 1998, 2000), to global warming (Thompson et al. 2000), and to stratospheric and oceanic processes (Shindell et al. 1999; Grotzner et al. 1998; Rodwell et al. 1999).

Although various phenomena of relatively long time scales, such as stratospheric and oceanic processes, can influence the tropospheric NAO, recent studies suggest that the intrinsic time scale of the NAO is about 10 days (Feldstein 2003). Furthermore, Feldstein (2000) showed that the amplitude time series for the NAO approximately follows a first-order Markov process. These results imply that the NAO can be interpreted as being a relatively short time scale stochastic process.

Given this short intrinsic time scale, Feldstein (2003) examined the daily evolution of the NAO life cycle using the streamfunction tendency equation, which essentially amounts to a vorticity budget analysis. He found that both high-frequency (period $<$ 10 days) and low-frequency (period $>$ 10 days) transient eddy fluxes drive the NAO anomaly growth. His results also suggest that the NAO decay is due to the combined influence of Ekman pumping and that of the low-frequency transient eddy fluxes.

While quantitative, the above composite results of Feldstein (2003) have limitations for providing the physical intuition necessary for advancing our understanding of the NAO. For example, the dominant role played by the eddy fluxes implies that the NAO life cycle is fundamentally a nonlinear process. Such behavior strongly contrasts that of the Pacific–North American Oscillation (PNA) life cycle, which is well described by linear processes (Cash and Lee 2001; Feldstein 2002). Because of this substantial role played by nonlinear processes, not surprisingly, as we will see, the

* Current affiliation: Department of Atmospheric Sciences, Colorado State University, Fort Collins, Colorado.

Corresponding author address: Dr. Sukyoung Lee, Dept. of Meteorology, The Pennsylvania State University, 503 Walker Building, University Park, PA 16802.
E-mail: sl@essc.psu.edu

© 2004 American Meteorological Society

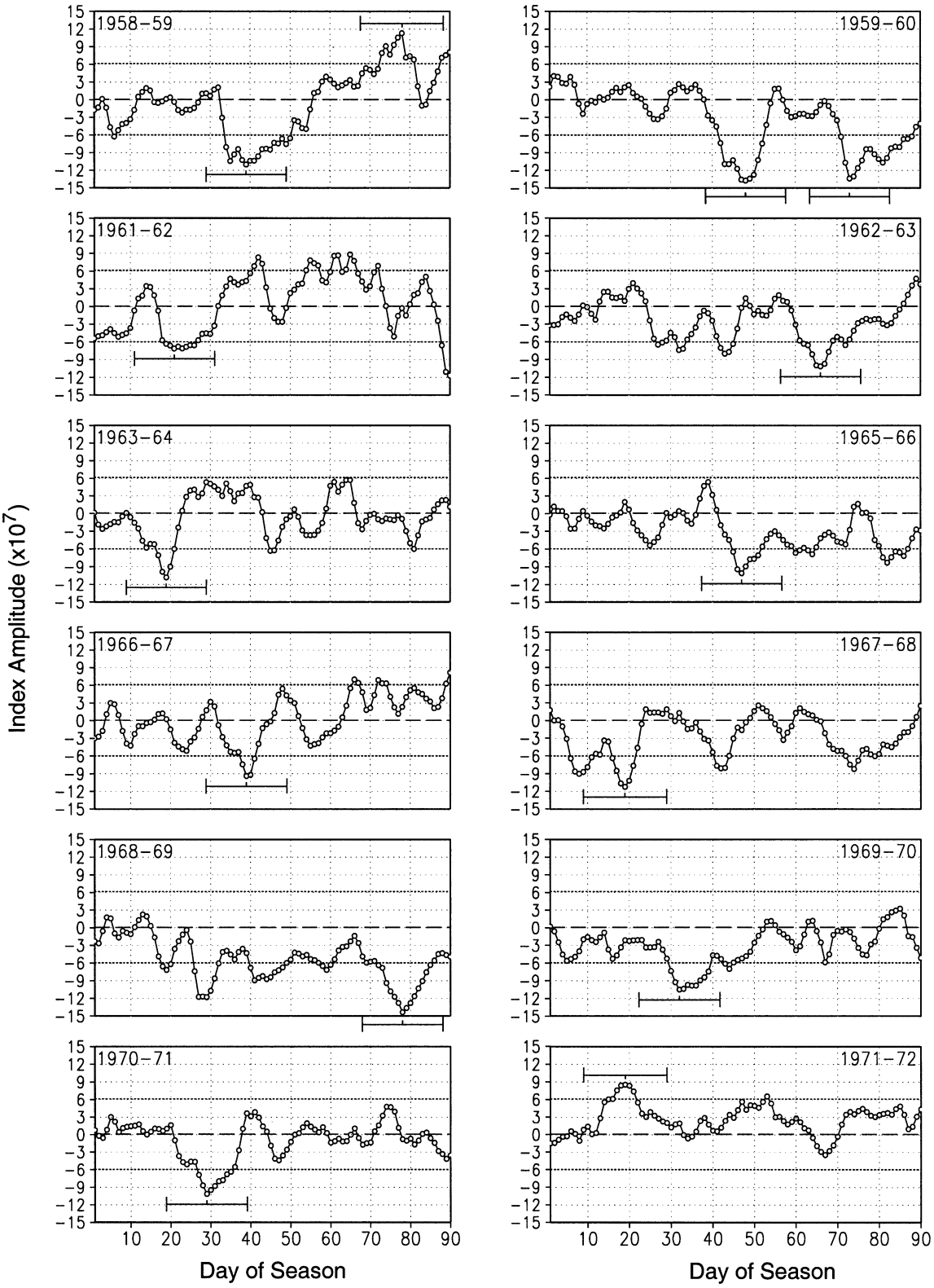


FIG. 1. The NAO index time series based on the first principal component of an RPCA analysis of the 300-mb geopotential height field. Each panel represents a 90-day winter season span. Only winter seasons in which selected NAO events occurred are shown; there were no events during the winters of 1964/65, 1980/81, and 1992/93. Selected positive and negative events are indicated by short line

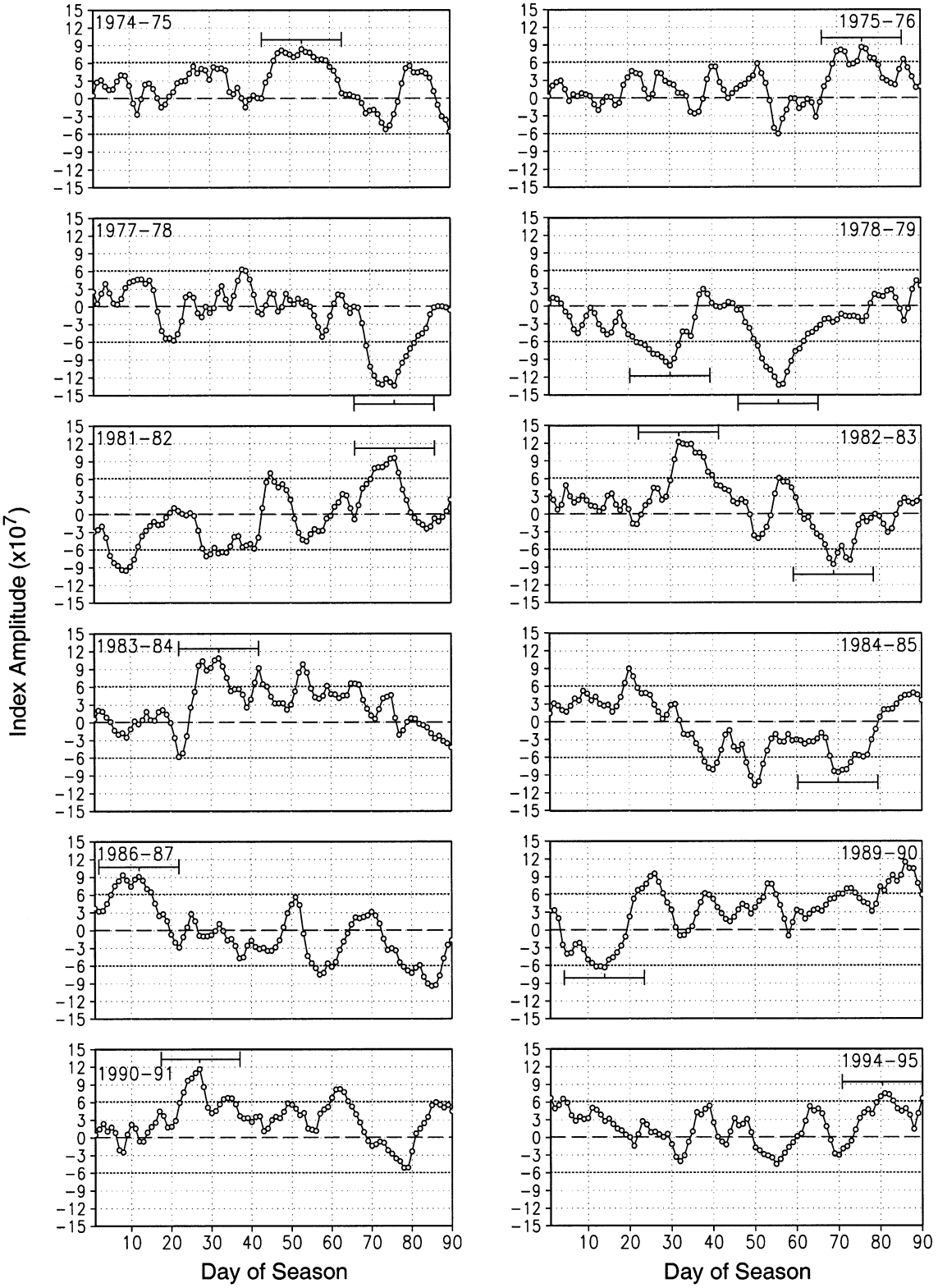


FIG. 1. (*Continued*) segments above or below the NAO index time series. The vertical axes represent the NAO index, the amplitude of which is arbitrary. The horizontal axes depict the day number within each season, and the year is shown along the top of each panel. The short-dashed lines represent the 1.33 standard deviation thresholds.

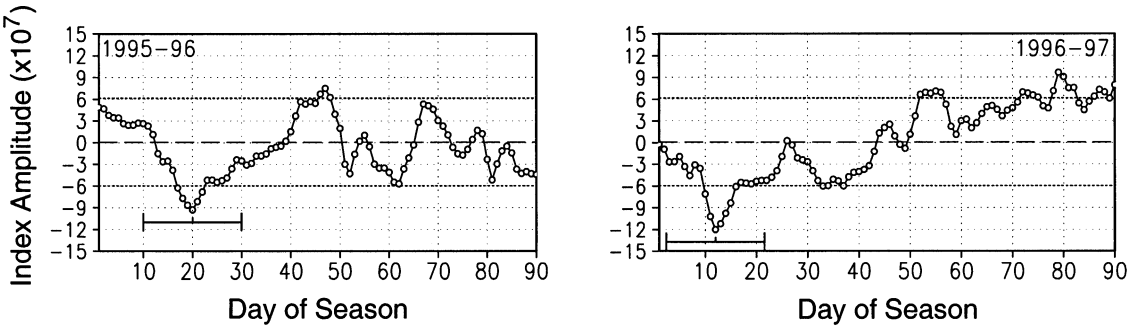


FIG. 1. (*Continued*)

NAO life cycle is closely linked to wave breaking and mixing of potential vorticity (PV). Given that wave breaking and mixing of potential vorticity occur at relatively small spatial scales, and exhibit much case-to-case variability, the spatial structures associated with wave breaking and mixing are not as apparent in composite fields as other variables, such as the eddy fluxes examined in Feldstein (2003). Therefore, to try to relate the above properties for the high- and low-frequency transient eddy fluxes to wave breaking and mixing, we examine the temporal evolution of potential temperature on the 2-PVU [1 potential vorticity unit (PVU) $\equiv 10^{-6}$ m^2 s^{-1} K kg^{-1}] surface, the nominal tropopause, on a case-by-case basis. Through the examination of a sufficiently large number of these events, our aim is to glean the essential dynamical properties of the NAO life cycle. We then present several cases that best illustrate those wave breaking and mixing characteristics that occur in each NAO life cycle.

The primary aim of this study is to obtain a simple morphological description of the dynamical processes that occur during the growth and decay of both phases of the NAO. This description focuses on the relationship between the transient eddy fluxes and the wave breaking and mixing since, as we will see, these two processes form the essence of the NAO life cycle. However, it is important to emphasize that an examination of why this wave breaking and mixing takes place is beyond the scope of this study. In addition, we aim to address a number of additional basic questions: 1) What physical entity does the NAO correspond to? 2) Why do low-frequency eddies first contribute toward NAO growth and then toward NAO decay? 3) What factors determine the approximate 10-day time scale of the NAO? 4) Why is the positive NAO phase preceded by a low-frequency wave train over the North Pacific, whereas the negative NAO phase develops in situ?[1] Furthermore, through a better understanding of the dynamics of the NAO on this shorter, intraseasonal time scale, it is possible that the results of this study will aid in our understanding of the NAO on the much longer interannual time scale.

Section 2 describes the data and analysis technique, and the results are presented in sections 3 and 4. A summary and conclusions follow in section 5.

2. Data and methodology

a. Data

Throughout this study, we examine the potential temperature field Θ on the 2-PVU surface, the so-called nominal tropopause. This quantity is chosen as our ''weather map,'' as it concisely displays the dynamical processes taking place in the upper troposphere and lower stratosphere. As this quantity is almost conserved at relatively short time scales, it is extremely useful for visualizing the entire flow evolution, including wave breaking (e.g., Thorncroft et al. 1993; Lee and Feldstein 1996). As we will see, our results will suggest that both phases of the NAO arise from the breaking of synoptic-scale waves. This wave breaking, which by definition corresponds to a reversal in the sign of the potential temperature or potential vorticity gradient, is easily visualized by examining potential temperature on the 2-PVU surface.

In general, a quantitative account of the relevant dynamical processes requires an inversion of the potential vorticity field (e.g., Davis and Emanuel 1991), so that the influence of surface theta and lower-tropospheric PV on the upper-tropospheric flow can be discerned. In this investigation, however, we concentrate only on the upper-tropospheric flow. This is because wave saturation and breaking, which are the main focus in this study, occur mostly in the upper troposphere and because these processes take place during the decay stage when the lower-tropospheric processes are mostly controlled by upper-tropospheric dynamics.

The daily maps of the Θ fields on the 2-PVU surface are derived from the daily (0000 UTC) National Centers for Environmental Prediction–National Center for Atmospheric Research (NCEP–NCAR) reanalysis wind

[1] It is important to note that this refers to in situ development of low-frequency eddies, not high-frequency synoptic-scale eddies. As will be presented later, for both NAO phases, the high-frequency wave trains are initially located upstream of the region where the low-frequency NAO anomaly develops.

and temperature data. The calculations are performed on a horizontal grid corresponding to a rhomboidal 30 truncation. The data covered by this study span the years 1958–97 for the months of December–January–February (DJF). The same dataset is also used for calculating the NAO-index time series described below.

b. Selection criteria

This study uses the results from Feldstein (2000) to specify the spatial pattern and principal component (amplitude) time series for the NAO. Therefore, we provide only a brief description of the calculation procedure. After removing the seasonal cycle, the NAO teleconnection pattern was obtained by applying a rotated principal component analysis (RPCA) to the 300-mb geopotential height field. In this study, the covariance matrix is used and a varimax rotation is applied to the truncated EOFs. We use the term ''NAO index'' to refer to the principal component time series.

The RPCA of Feldstein (2000) shows that the NAO spatial pattern is the first rotated empirical orthogonal function (REOF1) of the daily, unfiltered 300-mb geopotential height field (see Fig. 3a of Feldstein 2000). As shown in that study, REOF1 is described by the typical NAO dipole pattern, which consists of one center near southern Greenland and another broad center across the midlatitude North Atlantic.

A series of positive- and negative-phase NAO events are defined based on the principal component time series and a set of additional criteria. As a first step, we specify an event as a string of four or more consecutive days in which the NAO index is greater than 1.33 standard deviations. The day on which the index is at its largest value is defined as the *base point* of a particular preliminary event. We define an event as the 21-day period centered on the base point, hereafter labeled as the zero-lag day. Eleven events are discarded because of nonmonotonic growth and decay in which the NAO index, during the 21-day span, drops below the threshold and then rises back above that value as a secondary peak. Events that extend into non-DJF months are also discarded. The selected final events are presented in Fig. 1, which shows the daily NAO index time series. This time series indicates that a vast majority of the selected NAO events involve growth and decay periods on the order of 10 days, a result consistent with the findings of Feldstein (2000, 2003).

The resulting 10 positive and 20 negative NAO events[2] are analyzed closely. Using unfiltered fields, we produce two sets of composites aligned relative to the zero-lag day, one for all positive cases and the other for all negative cases. As we will illustrate in section 3, these composites capture all of the features that characterize the two NAO phases. In section 4, we will further analyze these fields by calculating anomaly fields and by applying high- and low-pass filters.

3. Synoptic description of NAO events

This section presents a synoptic description of a few selected NAO events for both phases. These examples exhibit the general upper-tropospheric features common to all of our selected NAO cases. One case will be for the positive phase and two cases for the negative phase. Our visual impression is that, while certain key characteristics are very robust for both phases, the negative NAO phase exhibits more event-to-event variability than the positive NAO phase. This difference between the two phases remains the case even when the selection criteria is relaxed to include more events. The first negative NAO example shows the initiation and termination of the anomaly, while the second negative NAO example presents one of the most spectacular cases of a possible high-frequency eddy feedback process.

As motivated in both sections 1 and 2, the following description will also emphasize wave breaking because of its important role in transforming synoptic-scale disturbances into the NAO. This transformation involves a change from a west–east orientation, normal for synoptic-scale wave trains, into a north–south dipole orientation, typical of low-frequency anomalies such as the NAO. Temperature advection associated with wave breaking is also emphasized because both our results and those of Franzke et al. (2003) show that the NAO can be described as a dipole anomaly in the potential temperature field.

a. An example of a positive NAO event

We highlight a typical positive-phase event by selecting the case whose zero-lag day is 27 December 1990 (see Fig. 1). Figure 2 shows the temporal evolution of Θ on the 2-PVU surface for this case. To aid the visualization of wave propagation, amplification, and breaking, values of Θ below 315 K are shaded. However, as this particular threshold value is not always the best choice for the purpose stated above, it is also helpful to examine other contours when examining wave breaking and amplification.

Between lag -10 and lag -7 days, we observe an amplifying ridge over the northeastern Pacific, resulting in a warm air cutoff near Alaska (see lag -6 day) and a tongue of cold air over western North America. The main body of cold air over Canada expands and is advected eastward into the North Atlantic between lag -6 and lag -2 days. At the same time, synoptic-scale waves develop over North America and migrate across the

[2] Examining the NAO index shown in Fig. 1, we attribute this asymmetry between the number of positive and negative events to the selection criterion that the NAO index must exceed 1.33 std dev for a string of four or more consecutive days. This asymmetry is consistent with the finding presented below that the negative NAO events resemble blocks that persist longer than nonblocking states.

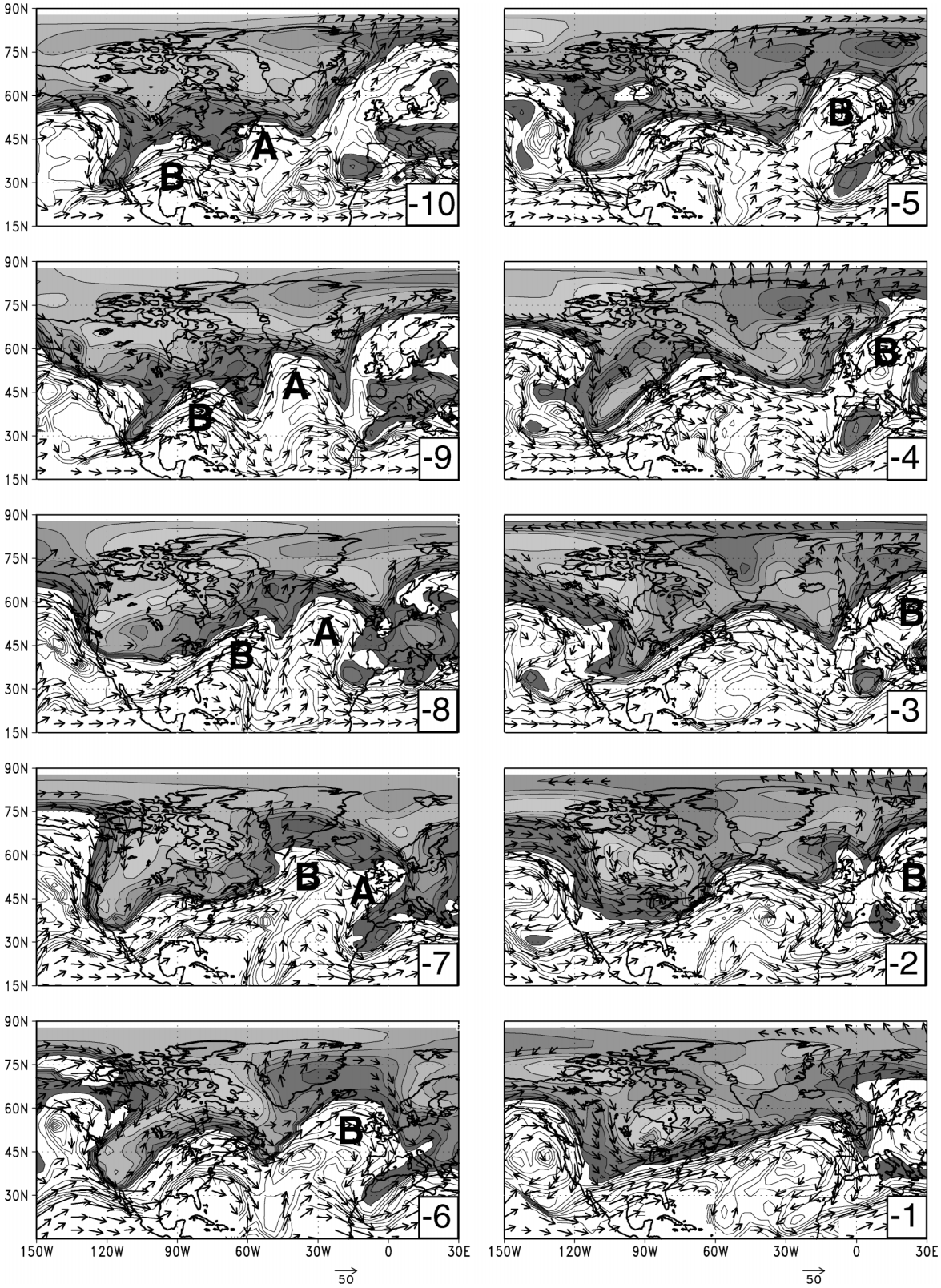


FIG. 2. Unfiltered Θ fields on the 2-PVU surface for the positive NAO event from Dec 1990. The Θ fields are contoured every 5 K and are shaded below 315 K. Darker (lighter) shading represents higher (lower) Θ values. The wind vectors are denoted by arrows. The corresponding lag days based on the peak NAO index value are shown to the right of each panel.

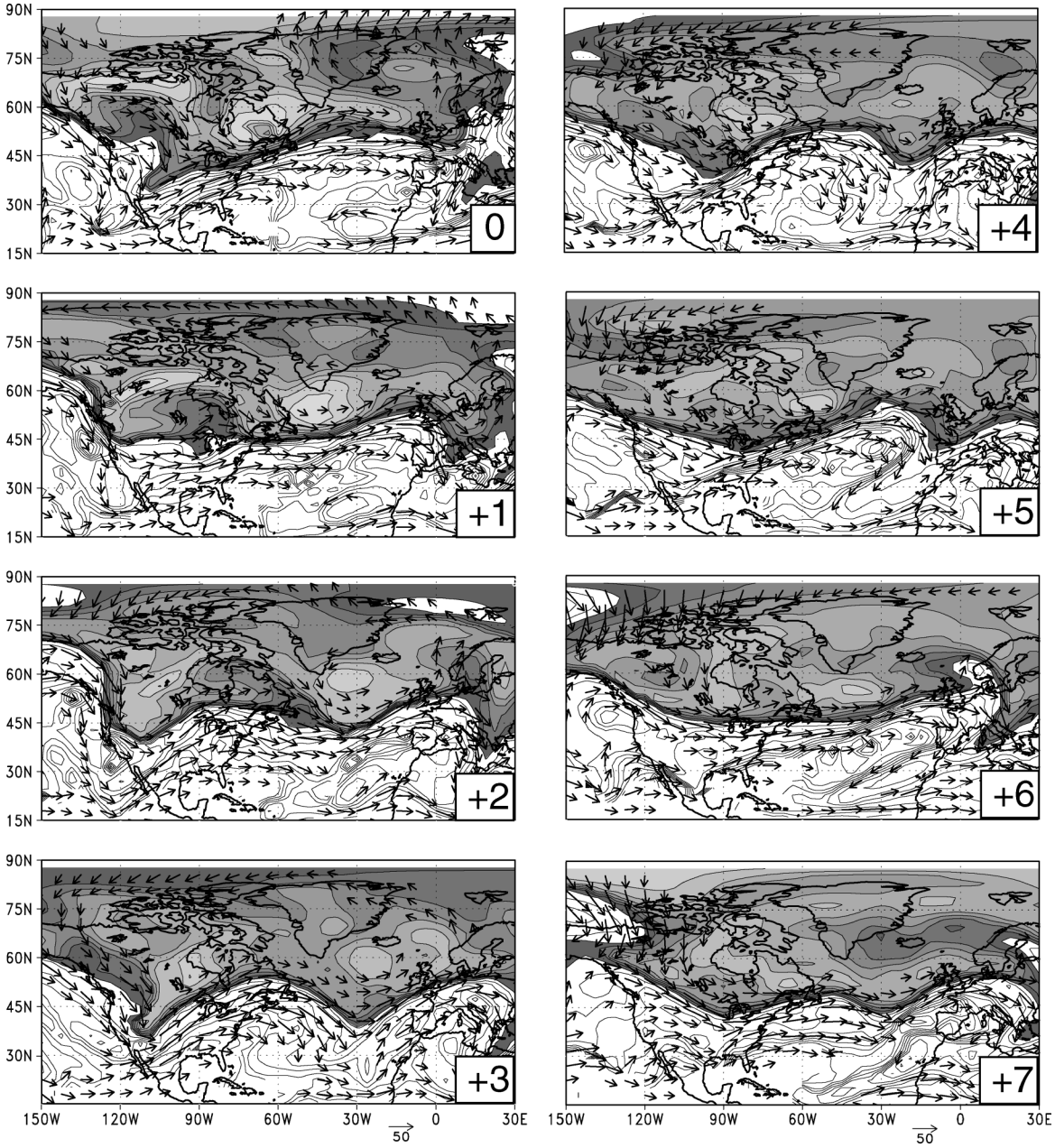


FIG. 2. (*Continued*)

North Atlantic. These waves, associated with ridges marked A and B, amplify, merge, and then break *anticyclonically*,[3] advecting warm air poleward over the central North Atlantic (see between lag −7 and −3 days). As a result of this warm advection and the above cold advection from Canada, the potential temperature gradient in the vicinity of the 315-K contour over the North Atlantic is tightened. This strengthens the westerlies, and establishes the positive phase NAO pattern. During the next several days (lag −1 to lag +7 days), similar wave breaking in the southern part of the NAO region and eastward cold air advection in the northern part of the NAO region is once again repeated, again intensifying the potential temperature gradient.

[3] In this study, we *broadly* follow Thorncroft et al. (1993) in defining anticyclonic and cyclonic wave breaking. Briefly, anticyclonic wave breaking is characterized by a southwest–northeast (SW–NE) tilted trough–ridge pair that is advected anticyclonically, and cyclonic wave breaking indicates a northwest–southeast (NW–SE) tilted trough–ridge pair that is advected cyclonically. As will be discussed below, most likely due to the zonally varying background flow, the morphology of these two wave breakings are somewhat different from that described by Thorncroft et al. (1993).

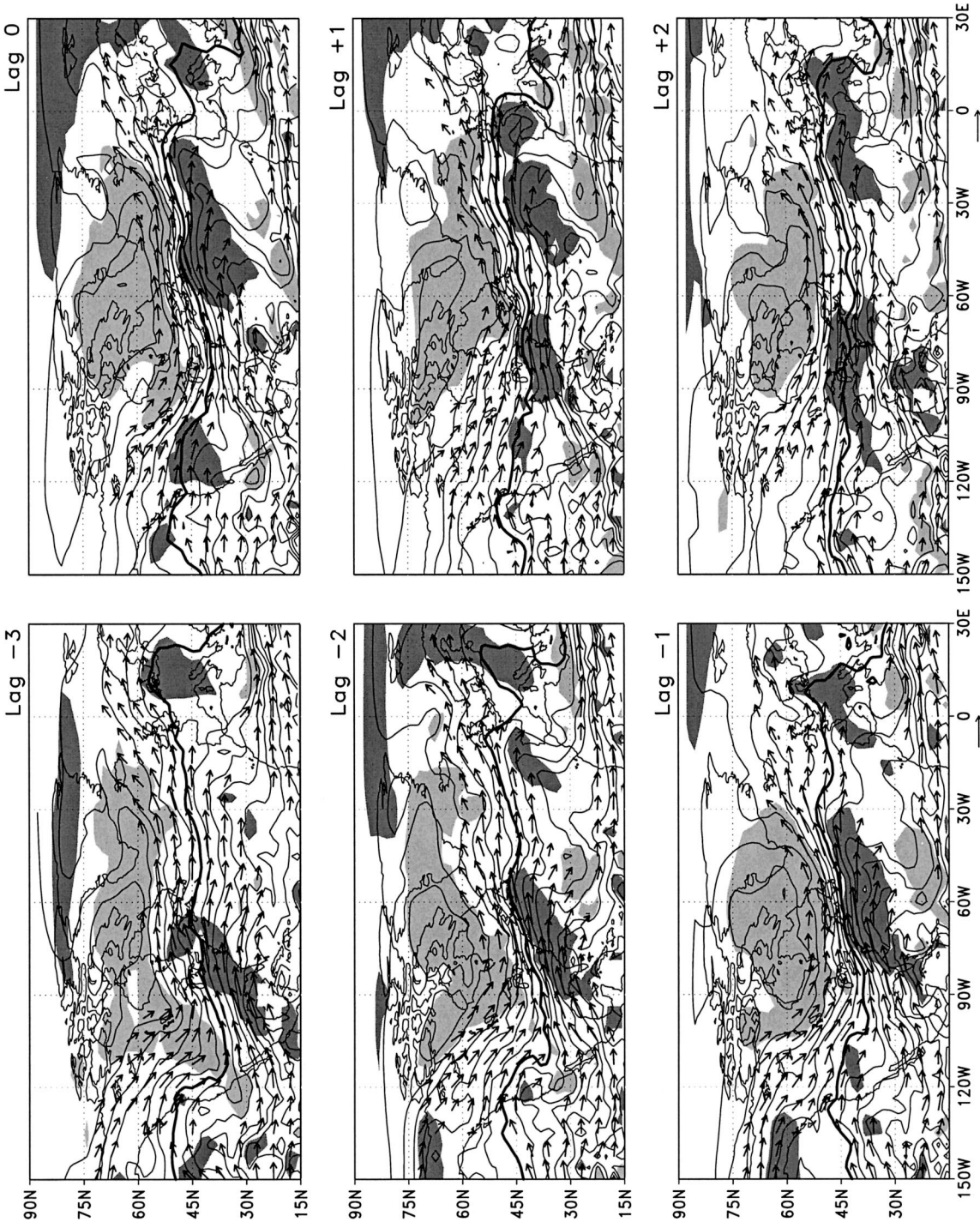


FIG. 3. A composite of unfiltered Θ fields from all 10 positive NAO events. The contour interval is 5 K, with the 320-K line emboldened to emphasize the low-over-high structure, the anticyclonic wave breaking, and the SW–NE tilt. Darker (lighter) shading denotes positive (negative) t values that exceed the 95% confidence level. The corresponding lag days are shown to the right of each panel. The wind vectors are denoted by arrows.

b. Composite wave breaking for the positive NAO phase

The above sequence of Θ fields suggests that anticyclonic wave breaking near the west coast of North America and over the North Atlantic is crucial for the growth, maintenance, and prolonging of the positive NAO state. Even in the composite field (see Fig. 3), the anticyclonic wave breaking over these regions is evident. The statistical significance of the composites is shown with shading in Fig. 3, which indicates potential temperature anomalies above the 95% confidence level. Since *t* statistics are used to determine the statistical significance, the shading in Fig. 3 indicates that the positive NAO phase is characterized by an anomalous low-Θ region over northeastern Canada, western Greenland, and the nearby North Atlantic, and a contrasting anomalous high-Θ zone across the central North Atlantic and western Europe. Thus, the spatial pattern of anomalous Θ field closely resembles that of the well known ''low-over-high'' geopotential height pattern of the positive NAO phase. This resemblance between the anomalous geopotential height and the 2-PVU potential temperature patterns for the NAO is examined in more detail by Franzke et al. (2003).

The relationship between the patterns of anomalous potential temperature and anomalous geopotential height allows us to link the dynamical processes presented in this study with the well-known low-over-high geopotential height pattern of the positive NAO phase. For example, Fig. 3 shows that the anomalous high (see lag −2 to lag +1 days) arises from the poleward intrusion of warm air associated with the anticyclonic wave breaking over the North Atlantic. Figure 3 also suggests that the anomalous low anomaly is associated with the southeastward advection of low-Θ air that follows the anticyclonic wave breaking in the northeastern North Pacific.

The above observations suggest that the positive NAO phase requires the occurrence of at least two breaking waves. As will be shown later, this behavior strongly contrasts that of the negative phase, which arises solely from the cyclonic breaking of a single wave confined to the North Atlantic.

The occurrence of this wave breaking over the northeast Pacific Ocean for the positive phase and the absence of wave breaking away from the North Atlantic for the negative phase likely explains why the positive NAO phase is preceded by a low-frequency wave train over the North Pacific and the negative NAO phase develops in situ (Feldstein 2003). The signature of the composite wave train, as seen by the 300-mb streamfunction anomaly (Feldstein 2003), can indeed be identified in Figs. 2 and 3: an anomalously strong trough in the central North Pacific and a pronounced ridge over the eastern North Pacific.

c. Example 1 of a negative NAO event

As stated above, the first negative NAO phase example is presented to illustrate the characteristics of the initiation and termination of the anomaly. The zero lag day for this case is 25 January 1979 (see the frame labeled 1978–79 in Fig. 1).

The sequence of Θ fields depicts the successive development of a North Atlantic ridge during the first segment of the event from lag −12 to lag −4 days (Fig. 4). Again, note that amplification and wave breaking can sometimes be better seen with contours rather than shading. Initially, a moderate amplitude North Atlantic ridge (marked C) propagates eastward between lag −12 and lag −10 days. By lag −7 days, another ridge, marked D, develops off the east coast of North America, propagates eastward, and once again forms a North Atlantic ridge. This time, however, the axes of the ridge and associated upstream trough tilt NW–SE, opposite to that of the positive phase (lag −4 days and onward). These flow characteristics are strikingly similar to that of blocks (Berggren et al. 1949; Palmen and Newton 1969; Shutts 1983; Hoskins and Sardeshmukh 1987).

The growth stage described above is similar to that of the other 19 selected negative cases, but its decay process is more striking than any of the other cases that we examined. In the second segment of the event (note that lag −3 to lag +4 days are not shown), from lag +5 to lag +11 days, a sharp decrease in synoptic activity occurs upstream of the blocklike North Atlantic pattern. The absence of upstream storms limits the deposition of high-Θ air into the North Atlantic ridge, leading to a slow, basinwide decay of the North Atlantic ridge. As can be seen between lag +6 and lag +11 days, low-Θ air is entrained eastward across the North Atlantic into the ridge, again resulting in the basinwide mixing within this region and the ultimate decay of the North Atlantic ridge.

Evidently, the above entrainment and mixing processes involve nonlinear interactions of quasi-stationary eddies. In fact, when the vorticity budget and projection analyses are performed on this particular event, as in the composites of Feldstein (2003), low-frequency transient eddy fluxes are found to play an important role for the decay of the anomaly (not shown). Further discussion on the generation and role of the low-frequency transient eddy fluxes will be presented in section 4.

d. Composite wave breaking for the negative NAO phase

A composite of unfiltered Θ fields on the 2-PVU surface for the 20 negative cases is presented in Fig. 5. As for the positive phase, shaded regions denote areas of statistical significance above the 95% confidence level. Again, the positive (negative) anomalous Θ values are associated with positive (negative) anomalous geopotential height values across the middle- and high-latitude

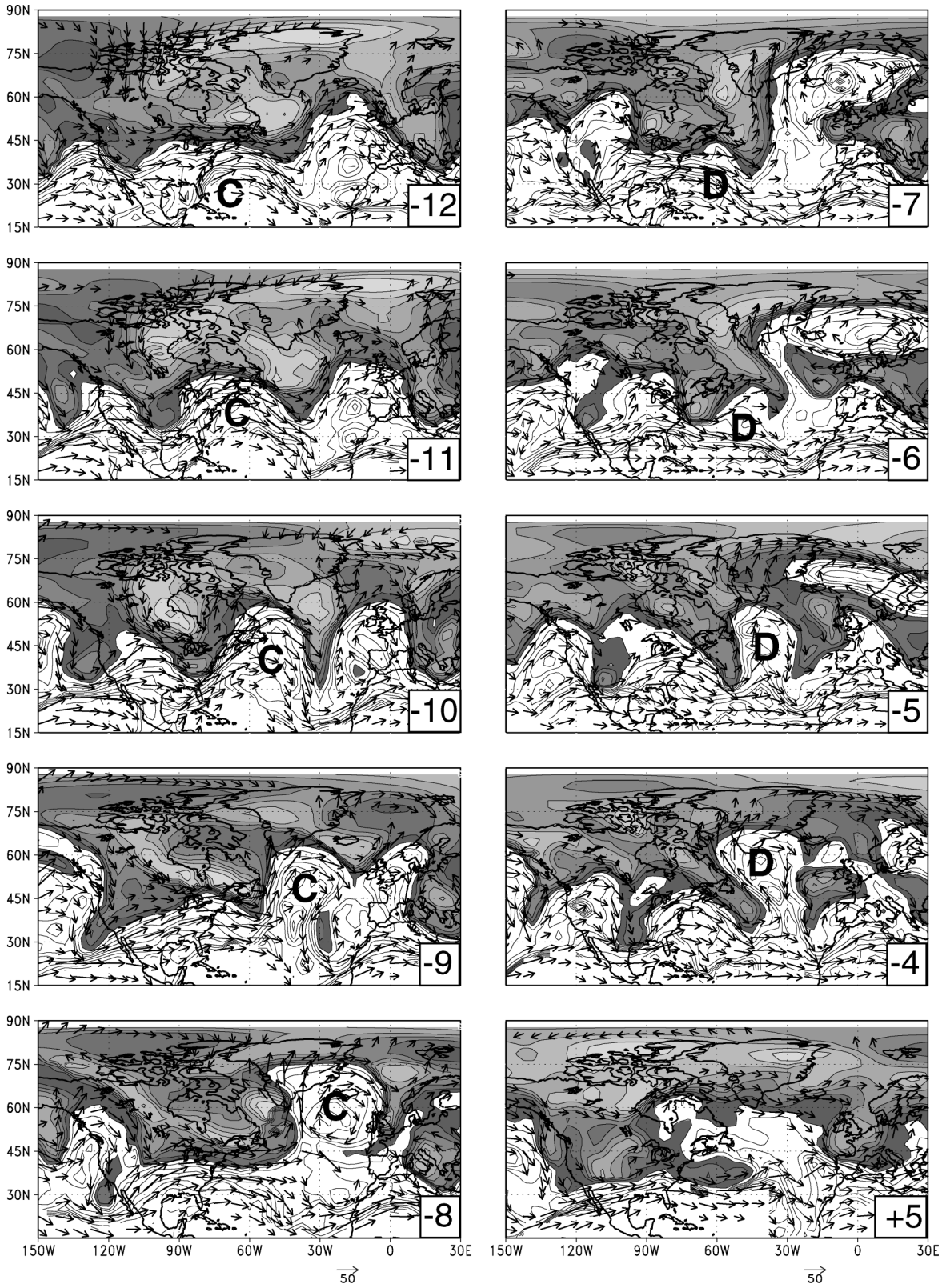


FIG. 4. Unfiltered Θ fields on the 2-PVU surface for a negative-phase NAO case from late Jan 1979. Shading schemes, vectors, and contour intervals are identical to those used in Fig. 2. Two periods, lag −12 to lag −4 days, and from lag +5 to lag +11 days, are presented.

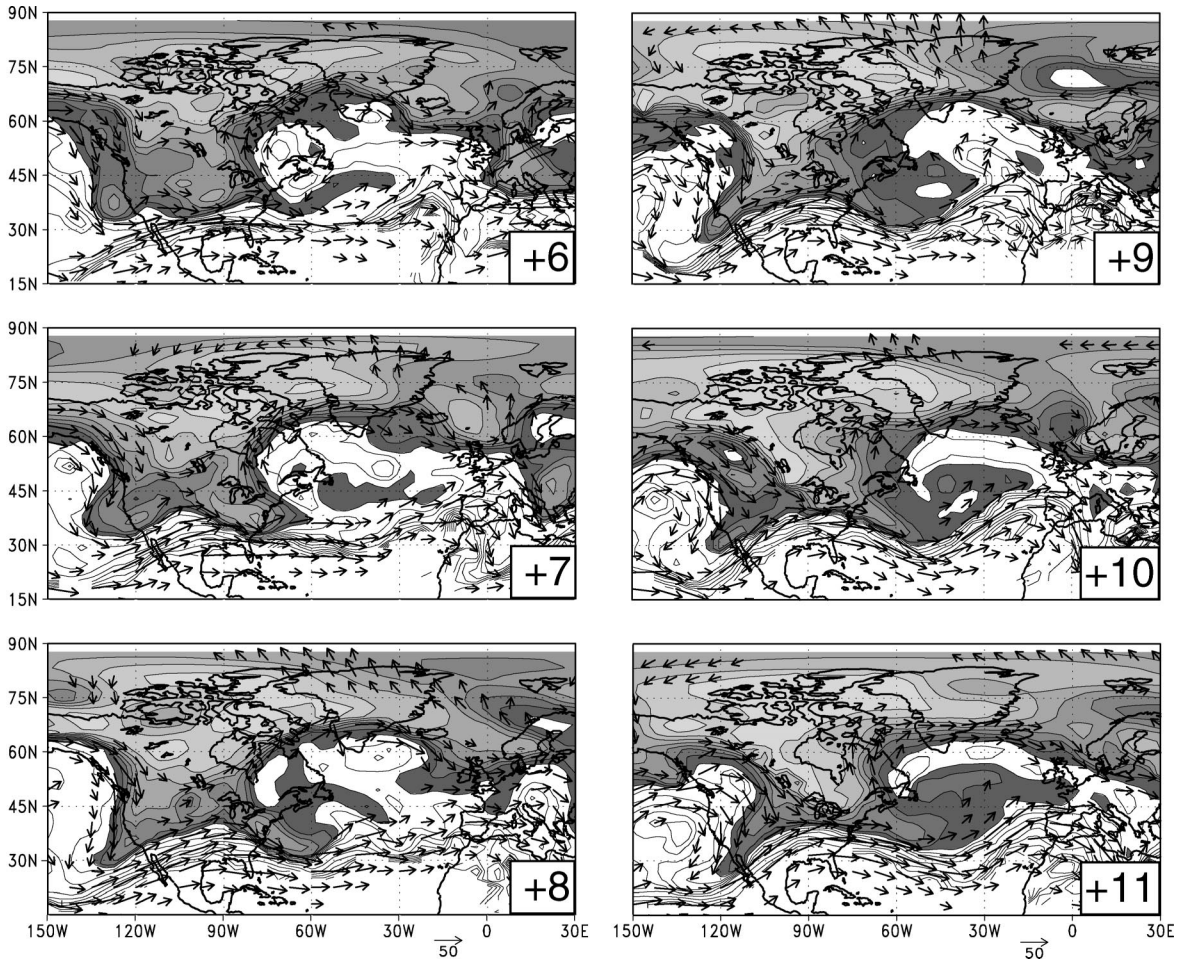


FIG. 4. (*Continued*)

North Atlantic. This ''high-over-low'' structure is seen as an amplified high-Θ anomaly centered over southern Greenland and a low-Θ anomaly extending across the midlatitude North Atlantic. We also observe the NW–SE tilt of the trough–blocking ridge combination in the western North Atlantic. As we have seen, these features are distinctly different from the general flow patterns of the positive phase. Negative NAO events, when compared to the positive phase, involve a more amplified blocklike ridge across the North Atlantic, a NW–SE tilt of the ridge–trough pattern, and cyclonic wave breaking of synoptic-scale eddies on the poleward side of the midlatitude jet.

The above cyclonic wave breaking, however, is different from that described by Thorncroft et al. (1993) where the cyclonic wave breaking is characterized by a broad, long lasting cyclonic vortex. For the negative phase of the NAO, instead of the cyclone, it is the NW–SE tilted anticyclone that is more prominant (e.g., see lag -1 in Fig. 5). Noting that the flow under consideration is the total flow, we suspect that this difference is due to the presence of the climatological background ridge over the North Atlantic. This speculation is consistent with the numerical model result of Franzke et al. (2003) that realistic NAO-like anomalies develop only when the zonally varying climatological flow is used as the background flow.

We can also relate the anomalous high and low geopotential height features of the negative NAO phase to the physical processes described above. For example, as can be seen in Fig. 5, the anomalous high arises from the poleward intrusion of warm air and the anomalous low is due to the equatorward advection of cold air. Both of these anomalies are associated with the same cyclonic wave breaking over the North Atlantic. There is some resemblance between the anomalous highs of the positive and negative phases in the sense that they both arise from wave breaking within the North Atlantic. However, the anomalous lows of the two phases bear much less resemblance, since the anomalous low of the positive phase is associated with wave breaking over the North Pacific, and the anomalous low of the negative phase results from wave breaking over the North Atlantic.

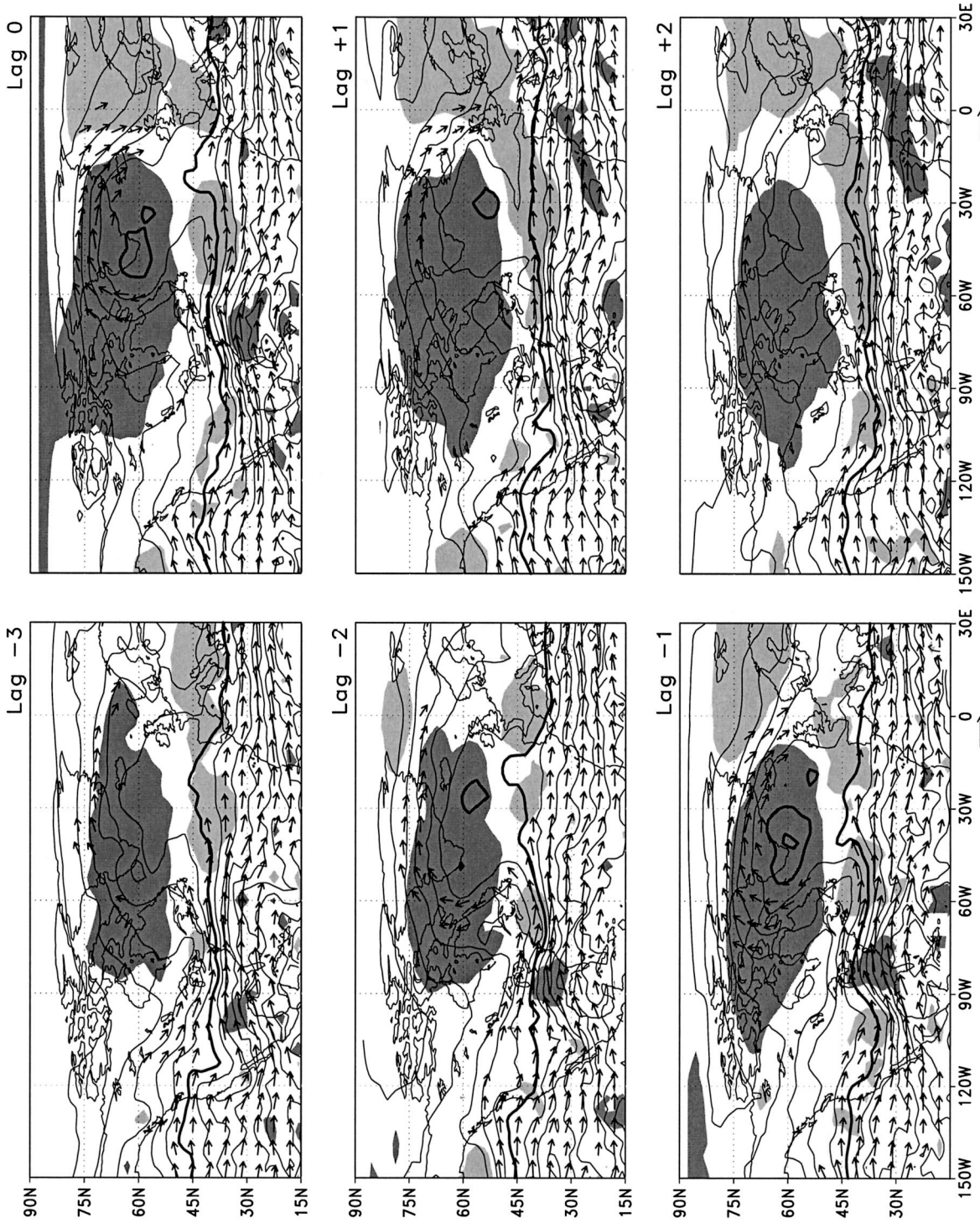


FIG. 5. A composite of unfiltered Θ fields from all 20 negative-phase events. Shading schemes, vectors, contour intervals, and confidence levels are identical to those used in the positive NAO composite of Fig. 3. The 320-K line is emboldened to illustrate the high-over-low structure, the cyclonic wave breaking, and the NW–SE tilt of the North Atlantic ridge axis.

e. Example 2 of a negative NAO event

While example 1 illustrates synoptic features during the onset and decay of negative NAO events, the second example, to be described below, shows a rather extreme case where the event is maintained by the repeated breaking of synoptic-scale waves. The zero-lag day for this case is 19 December 1967.

As can be seen in Fig. 1, lag −11 days of this event corresponds to a local maximum for this negative NAO case. Consistently, a robust ridge has already developed in the central North Atlantic several days prior to the defined starting day of the event (lag −10 days, not shown) and persists through lag −8 days (see Fig. 6). The initial growth process responsible for the preexisting North Atlantic ridge is very similar to that for the first negative-phase NAO example.

Distinct synoptic-scale wave breaking events occur along the western edge of the North Atlantic ridge. The first of these wave breaking sequences occurs between lag −8 and lag −4 days. The cyclonic wave breaking of the ridge, marked E, combines with this preexisting high-Θ region to broaden the ridge over the North Atlantic. A similar sequence of synoptic-scale eddy development, advection, cyclonic wave breaking (see F in lag −3 days and onward), and ridge strengthening can be seen between lag −2 and lag +1 days in Fig. 6. Therefore, we observe synoptic-scale eddies contributing to the maintenance of persistent Θ anomalies.

f. Summary

Schematic depictions of the time evolution of the positive and negative NAO phases appear in Figs. 7 and 8, respectively. Each frame represents the general atmospheric structure approximately every 3 to 5 days during an NAO event, with Figs. 7c and 8c depicting the circulation patterns when the NAO index is at its extreme value. It is important to note that the thick contours are the *total flow*, with the northern (southern) contour corresponding to ≈305 K (≈335 K). The warm and cold air indicated in these figures are *anomalies.*

The positive phase of the NAO is the remnant of two consecutive anticyclonic wave breakings, one near the west coast of the North America and the other over the subtropical North Atlantic. The beginning of the positive NAO phase (Fig. 7a), corresponding roughly to lag −8 days, is marked by the development of a robust Pacific ridge together with a trough off the west coast over the North America. The structure of this trough and ridge hint at the initiation of wave breaking. Also, at this stage, a much weaker ridge and trough are present over the central North Atlantic.[4] The two dashed lines in Figs. 7a and 7b indicate the location of the trough axes. As these waves propagate toward the east, the Pacific ridge and western North American trough break anticyclonically, expanding the cold air southeastward (see the change in the location of the northern contour between Figs. 7a and 7b.) The main body of the cold air continues of strengthen, perhaps due to diabatic cooling, and moves into eastern Canada and Greenland (Fig. 7c).

Following this upstream wave breaking, the trough–ridge system over the downstream North Atlantic also starts to break anticyclonically (Fig. 7b), advecting warm air originally over Florida (see Fig. 7a) into central North Atlantic (Fig. 7c). This latter wave breaking takes place mostly along the southern contour. Consequently, as the cold anomaly over Canada moves over the North Atlantic, the ''cold-over-warm'' pattern of the positive NAO is established. The warm anomaly pinched off from the Pacific ridge also contributes toward this positive NAO pattern (Fig. 7c). If there is no additional wave breaking to replenish the north–south dipolar NAO anomaly, this pattern gradually decays (Fig. 7d).

In contrast to the positive phase, the negative phase of the NAO is the remnant of a single cyclonic wave breaking over the North Atlantic (Fig. 8). This is not surprising given that only a single wave breaking, regardless of the tilt, is needed to create a high-over-low (i.e., warm-over-cold) anomaly. With little upstream influx of synoptic-scale waves, this negative NAO pattern will slowly decay through a basinwide, low-frequency mixing process (Fig. 8d), as can be seen between lag +6 and lag +11 days in Fig. 4 and from lag +1 to +4 days in Fig. 6. With sufficient upstream activity, however, a resurgence of high-Θ air associated with the synoptic-scale eddies may revitalize the North Atlantic ridge (see lag +6 days of Fig. 6).

4. Wave breaking and generation of the low-frequency transients

As motivated in sections 1 and 2c, this section attempts to gain insight into how low-frequency eddies are generated and why the low-frequency eddy fluxes first contribute to the growth, but later to the decay, of the NAO (Feldstein 2003).

Concerning the question of how the low-frequency transient eddy fluxes contribute to NAO anomaly

[4] This pattern is consistent with the low-frequency wave train shown in Feldstein (2003, see Fig. 2b of that paper), but it is unclear how this low-frequency wave train forms. Our visual impression from the cases we examined (e.g., see Fig. 2) suggests that this low-frequency wave train originates from the breaking of synoptic-scale waves. This possibility is consistent with the results of Feldstein (2003) and Franzke et al. (2003). Feldstein (2003) shows that driving by high-frequency transient eddies contributes to the development of this low-frequency wave train. Franzke et al. (2003) obtain a similar low-frequency wave train in their initial value problem when their initial perturbation is comprised only of a high-frequency wave train. However, these results do not rule out the possibility of tropical convection playing a role.

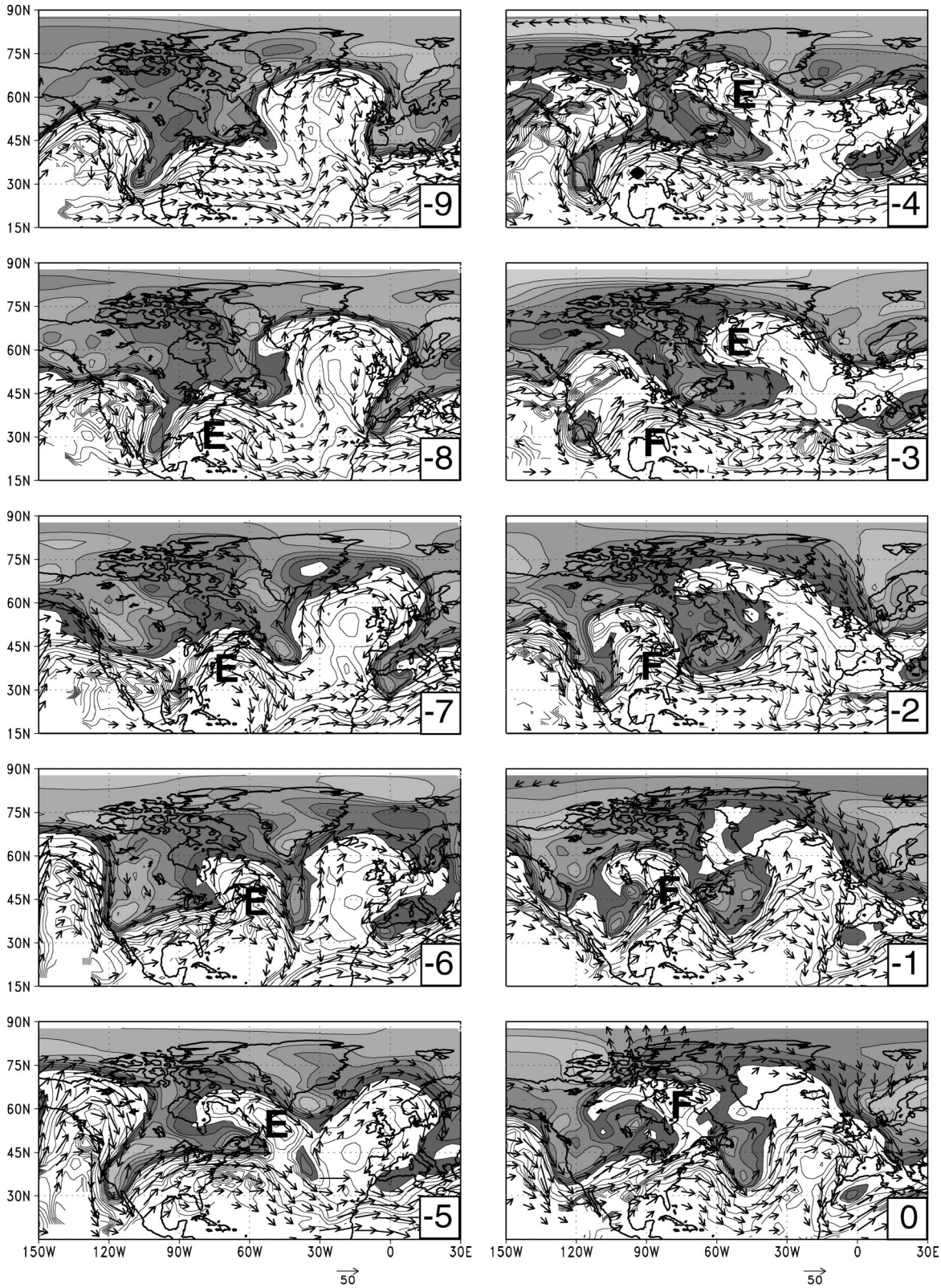


FIG. 6. Unfiltered Θ fields on the 2-PVU surface for a second negative-phase NAO case from Dec 1967. Shading schemes, vectors, and contour intervals are identical to those used in Fig. 2.

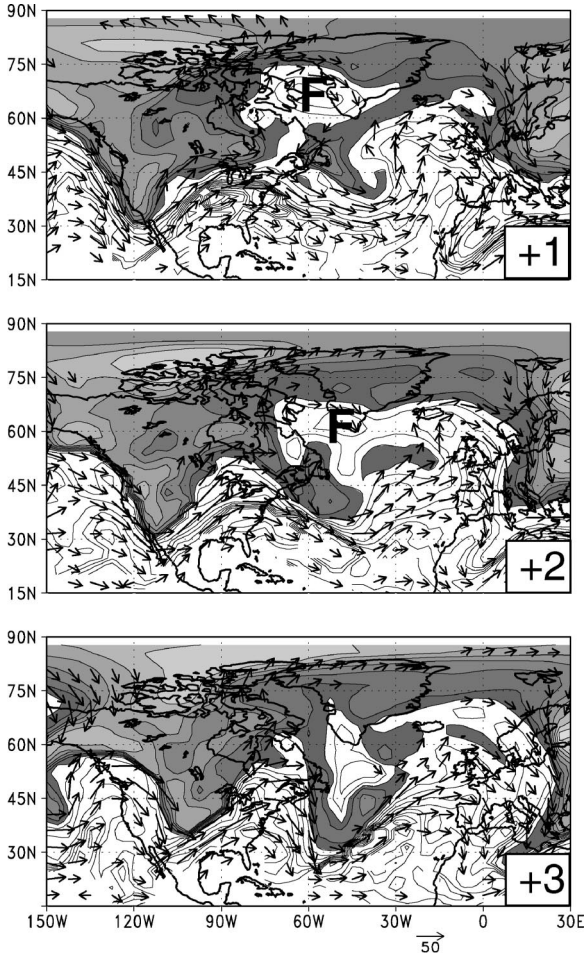


FIG. 6. (*Continued*)

growth, it is useful to reexamine Figs. 2 and 6, focusing on the change in the propagation speed of the synoptic-scale waves entering the North Atlantic. In particular, following the time evolution of the high-Θ air, marked by A and B in Fig. 2 and E in Fig. 6, it can be seen that the eastward propagation speed lessens as the disturbances propagate into the North Atlantic. This deceleration always accompanies wave breaking (anticyclonic for the positive phase, cyclonic for the negative phase) and an increase in the zonal scale. Such a lengthening of the zonal scale is a feature of low-frequency eddies (Hoskins et al. 1983). This behavior suggests that, at least for the NAO, low-frequency eddies are generated as a result of the breaking of high-frequency waves. In fact, such a generation mechanism of low-frequency eddies was previously suggested by Swanson et al. (1997) through their idealized model calculations.

As a first step to quantify the above visual impression, the total flow anomalies corresponding to Figs. 2 and 6 are decomposed into high- and low-frequency contributions. One anticipates that the total anomaly fields will first more closely resemble the high-frequency fields, followed by a greater similarity with the low-frequency fields. To decompose the total anomaly fields into the two frequency ranges, for each Northern Hemisphere (NH) winter season, a Fourier filter is applied to the 2-PVU Θ field with a cutoff frequency of 10 days. Because the 2-PVU Θ field is often undefined at low latitudes where the potential vorticity surface becomes increasingly vertical, for a given gridpoint, if the value of Θ is undefined on more than three consecutive days, we do not perform the Fourier analysis and issue a missing flag. Otherwise, the undefined values are estimated with linear interpolation of the surrounding values, and the Fourier decomposition is applied to this new time series.

a. The positive-phase example

We present the total anomaly, high-frequency, and low-frequency Θ fields from lag −8 to lag −3 days for the NAO positive example shown in Fig. 2 (see Fig. 9). This 6-day span focuses on the wave breaking sequence involving the A and B high-Θ regions described in Fig. 2. Initially at lag −8 days, the circled Θ anomaly, which corresponds to A in Fig. 2, is primarily a high-frequency feature and projects poorly onto the low-frequency Θ field (see Fig. 9). The circled anomaly corresponding to A and then B (see Fig. 2 at lag −6 days, when ridges A and B merge) evolves slowly into a low-frequency feature from lag −7 to lag −3 days. This observation is consistent with the initial rapid movement of the high-Θ air of region A, the merger of A and B, and then the slow anticyclonic wave breaking that occurs from lag −5 days onward.

b. The negative-phase example

The anomaly, high-frequency, and low-frequency Θ fields from lag −8 to lag −3 days for example 2 of the negative NAO phase are presented in Fig. 10. This sequence of Θ fields focuses on the first wave breaking evolution (denoted by E) previously described in the unfiltered Θ fields of Fig. 6. Although the wave breaking processes seen in this event differ from those of the positive phase, we observe similar frequency transitions in the Θ anomaly fields. Initially at lag −8 days, the high-frequency Θ pattern in the circled region more closely resembles the total anomaly than does the low-frequency pattern. Over the next five days, as the cyclonic wave breaking takes place, we note that the similarity between the high-frequency Θ features and the total Θ anomaly in the circled region steadily decreases, while the similarity between the total and low-frequency anomalies increases. At lag −3 days, the Θ anomaly in the circled region (representing the high-Θ air incorporated into the ridge as seen in Fig. 6) projects cleanly onto the low-frequency pattern; in contrast, the high-frequency Θ pattern is noticeably dissimilar to the same circled anomaly.

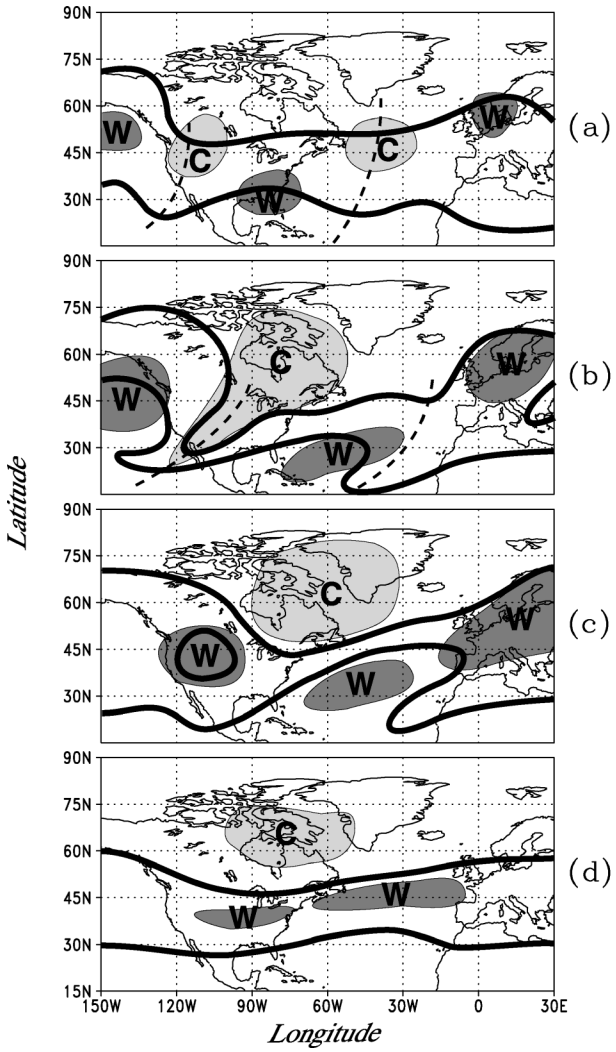


FIG. 7. (a)–(d) A schematic diagram depicting the generalized features and flow patterns of the positive NAO phase. Each frame captures the atmospheric features on 3–5-day increments, with (c) representing the zero-lag day. The thick contours are for the total flow, with the northern (southern) contour corresponding to ≈305 K (≈335 K). The warm and cold air indicated in this figure correspond to anomalies. The dashed curves indicate the trough axes.

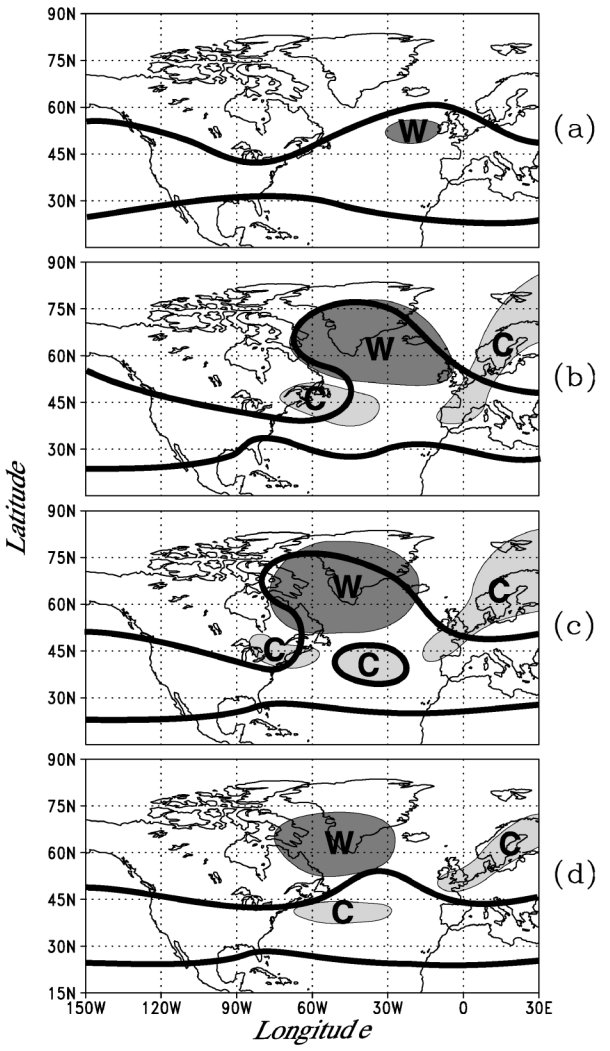


FIG. 8. (a)–(d) A schematic diagram depicting the generalized features and flow patterns of the negative NAO phase. As in Fig. 7, the time increment of each panel is approximately 3–5 days, with (c) again representing the atmospheric features corresponding to the zero-lag day.

c. Summary

In order to further quantify the high-to-low frequency transition of the anomalies, we perform the following calculations. We first compute the projection of both the high-frequency and low-frequency Θ fields onto the total Θ anomaly field in the domain covering 20°–90°N, 120°–60°W. This results in the generation of two time series. Lag correlations between these two time series are then computed. The resulting lag correlations for the 10 positive and 20 negative cases are presented in Figs. 11a and 11b, respectively. The individual positive and negative NAO cases corresponding to Figs. 2 and 6, respectively, appear as thick, dashed lines in the lag correlation plots. In both cases, the low-frequency projection lags the high-frequency projection by between one and two days. This result is consistent with the visual impression given by Figs. 9 and 10. As can be seen in Fig. 11, similar behavior is found in most of the cases that we examined. The maximum values observed in the composite lag correlation profiles (thick, solid lines) are statistically significant above the 99.9% confidence level for both positive and negative phases (0.37 and 0.39, respectively). The information conveyed by these graphs, together with the results in Figs. 9 and 10, suggests that the high-frequency synoptic-scale systems that propagate into the North Atlantic region and undergo wave breaking also serve as a transition to lower frequencies.

d. Interpretation of the streamfunction budget analysis

As motivated earlier, we next examine whether the above synoptic evolution can be used to interpret the streamfunction budget analysis of the composite NAO life cycle (Feldstein 2003). For this purpose, we apply the projection technique of Feldstein (2003) to the individual events illustrated in Figs. 2 and 6. Thus, we calculate the projections of various terms on the right-hand side of (A1) onto the streamfunction anomaly at the zero lag day (see appendix A). Figure 12a shows the projections for the positive phase event of Fig. 2. As the driving by the high- and low-frequency transient eddy fluxes dominates the projections, only the influence of these terms is illustrated. As can be seen in Fig. 12a, during the growth stage, the NAO anomaly is first driven by high-frequency transient eddy fluxes and then by the low-frequency transient eddy fluxes. During the decay period, the high-frequency eddy fluxes prolong the lifetime of the NAO anomaly, while the low-frequency eddy fluxes act to dampen the NAO anomaly. These results for this individual case are qualitatively very similar to those for the composite NAO life cycle (see Fig. 6 of Feldstein 2003). For the negative phase, the properties of the projections shown in Fig. 12b resemble those in Fig. 12a and also that of the composite NAO life cycle for the negative phase (see Fig. 7 of Feldstein 2003).

This resemblance between the projections for the cases in Figs. 2 and 6, and those of the composite NAO life cycle, supports the statement in section 2b that these cases capture the essential features of both NAO phases. Furthermore, the results from these projections make a link between the high- and low-frequency eddy fluxes of the streamfunction tendency equation (see appendix B) and the wave breaking that takes place in each of the examples of this study. In particular, the projections allow us to relate four aspects of the wave breaking to the roles played by the transient eddy fluxes. These are 1) the initial driving by high-frequency transient eddy fluxes corresponds to the early stage of the wave breaking process when the initial synoptic-scale disturbance begins its nonlinear evolution into the NAO pattern, 2) the prolongation of the NAO event by the high-frequency transient eddies is consistent with the replenishment of the NAO pattern by subsequent upstream synoptic-scale disturbances, 3) the driving of the NAO by the low-frequency transient eddy fluxes corresponds to the later stage in the wave breaking process when filamentation and shedding take place, and 4) the damping by the low-frequency transient eddies during the NAO decay arises from the mixing that takes places at the end of the NAO life cycle. The fourth point can be seen by examining the Θ field during the decay period indicated by the projections. For example, for the negative phase, during the decay period between lag 0 and lag +5 days (see Fig. 12b), Fig. 6 shows the North Atlantic flow characterized by notable filamentation and shedding of low-Θ air into the high-Θ air. A more spectacular example of this low-frequency wave breaking and mixing was noted earlier in example 1 for the negative NAO phase (See the time period between lag +6 and lag +11 days in Fig. 4.) During this period of mixing, the projections indicate that low-frequency transients act to decay the NAO anomaly (not shown).

5. Discussion and conclusions

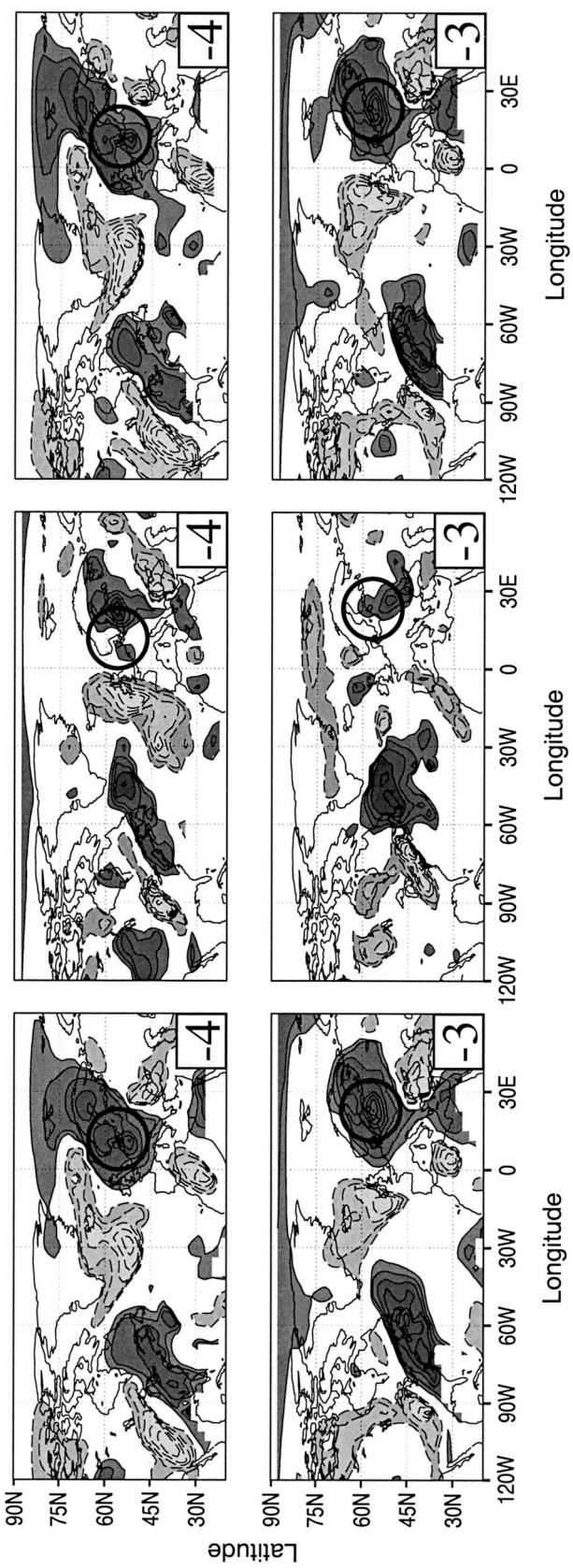
As a continued effort to try to understand the NAO, this study examines the daily evolution of the potential temperature field on the nominal tropopause for individual NAO events. We find that the positive NAO events are characterized by an anticyclonic breaking of synoptic-scale waves, exhibiting a SW–NE tilt. In contrast, the negative NAO events are characterized by cyclonic breaking of synoptic-scale waves with a NW–SE tilt. For the positive phase there are two anticyclonic wave breakings and for the negative phase there is a cyclonic wave breaking. The negative NAO events share a close resemblance to blocking events, and this result is consistent with the statistics pointed out by Shabbar et al. (2001) that most blocking events take place during the negative NAO phase.

This study provides some insight into a physical process of low-frequency flow generation (see also Swanson et al. 1997) and helps us to address the first three questions raised in the introduction.

1) Upstream of the NAO region, transient waves first appear as high-frequency eddies. As these waves propagate into the NAO region, their eastward propagation speed lessens, the waves break, and they increasingly project onto low frequencies (see Fig. 11 for a summary). Thus, we conclude that it is the remnants of this wave breaking that form the physical entity of the NAO.
2) While the supply of upstream high-frequency eddies lasts, as these eddies break, they become part of the NAO pattern. When there is no longer an influx of high-frequency eddies, the wave breaking continues without replenishment. This stage, which is characterized by mixing of the low-frequency eddies, coincides with the NAO decay. This nonlinear wave evolution explains why low-frequency eddies first contribute toward the growth and then the decay of the NAO (Feldstein 2003).
3) The above results suggest that the NAO time scale is not only determined by a high-frequency eddy feedback and by spindown through Ekman pumping (Feldstein 2003), but also by the mixing time scale associated with the wave breaking.

The fourth question of the introduction can be addressed by first recalling that the positive NAO phase requires the occurrence of two breaking waves, whereas for the negative phase it is necessary that there is only


Total PT Anomaly
High-frequency PT
Low-frequency PT
-8
-7
-6
-5
90N
75N
60N
45N
30N
120W
90W
60W
30W
0
30E
Latitude



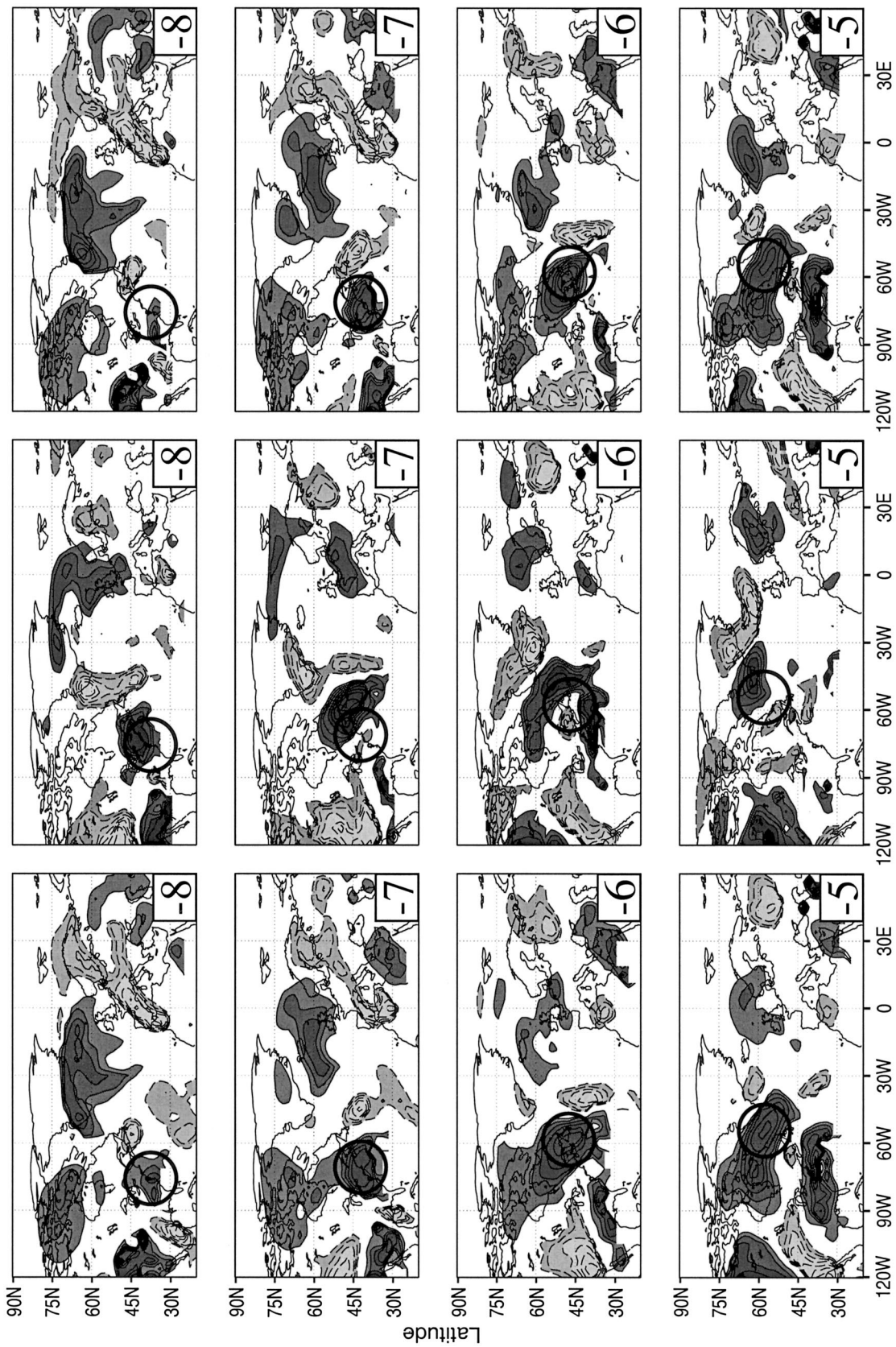
one breaking wave. One can understand these differences by noting that both cyclonic and anticyclonic wave breaking result in the occurrence of dipole anomalies with the positive center always lying poleward of the negative center.[5] These kinematics imply that a single cyclonic wave breaking event can easily generate the high-over-low anomaly structure of the negative NAO phase (Fig. 8c), but that a single anticyclonic wave breaking event cannot generate the low-over-high structure of the positive NAO phase (Fig. 7b); for the latter phase, the low comes from anticyclonic wave breaking of the *northern* contour near the west coast of North America, while the high arises from anticyclonic wave breaking of the *southern* contour over the subtropical North Atlantic. Provided that the low-frequency anomalies are indeed remnants of these wave breakings, as evidenced by this study (Figs. 10 and 11), the above difference in wave-breaking characteristics between the two phases of the NAO is a likely explanation as to why the positive NAO phase is preceded by a low-frequency wave train over the North Pacific and the low-frequency anomalies of the negative NAO phase develop in situ.

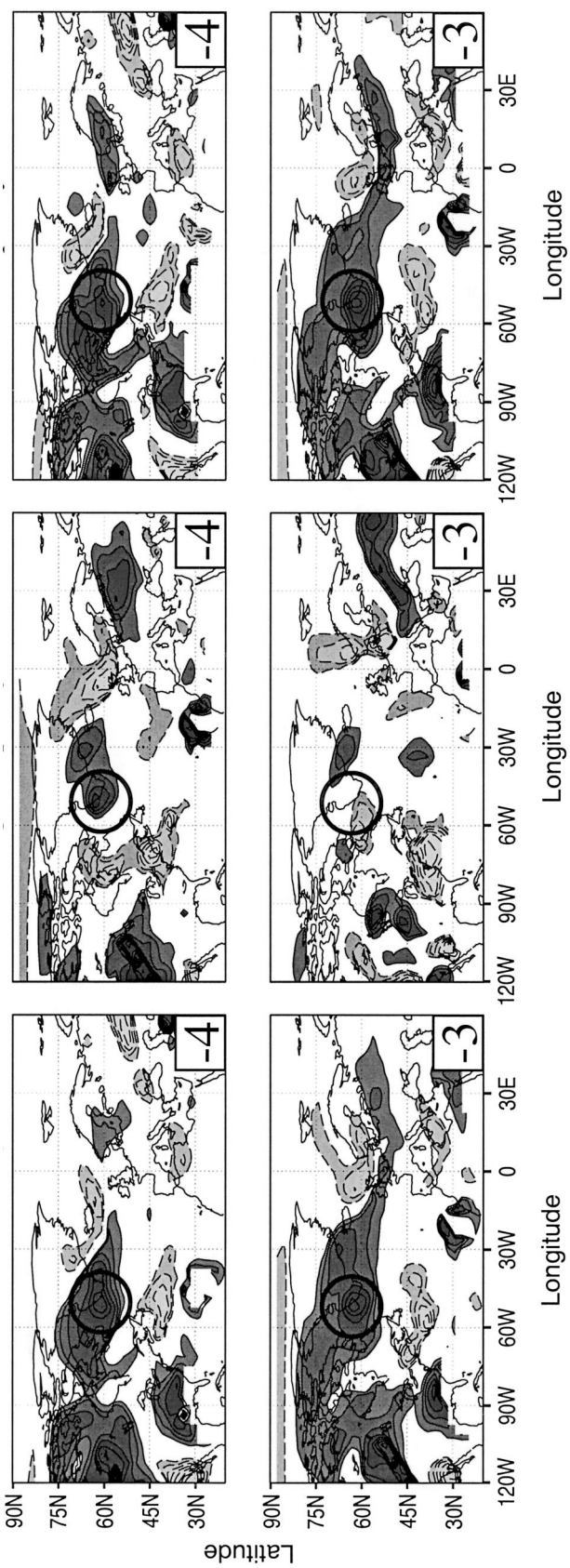
The prominent role played by synoptic-scale transients and their nonlinear interactions supports the view that the NAO can be, to lowest order, thought of as a stochastic process arising from turbulent synoptic-scale fluctuations. Still, one may question what are the major factors that determine anticyclonic versus cyclonic wave breaking, and thus the phase of the NAO. Simmons and Hoskins (1980) and Thorncroft et al. (1993) have shown that the manner in which waves break exhibits a high degree of sensitivity to the meridional shear of the basic-state zonal winds. In a separate study (Franzke et al.

[5] For the positive phase, see the anomalies associated with each of the two contours in Fig. 7b, but note that there is no noticeable warm anomaly over northwestern North America associated with the northern contour. This is due to the fact that there is a climatological ridge in that region. For the negative phase, see the anomalies associated with the northern contour in Fig. 8b.

←

FIG. 9. Total anomaly, high-frequency, and low-frequency Θ fields from lag −8 to lag −3 days of the positive NAO case depicted in Fig. 2. The thick, solid circle indicates the location of the total Θ anomaly corresponding to the merging of A and B in Fig. 2. Solid contours and darker shading in the total Θ anomaly (left column) represent values more than 10 K above the mean, with dashed lines and light shading indicating anomalies more than 10 K below the mean (5-K interval). Solid contours and darker shading in the high-frequency Θ field (middle column) represent values more than 4 K above the mean, with dashed lines and lighter shading indicating values more than 4 K below the mean (2-K interval). Solid contours and darker shading in the low-frequency Θ field (right column) represent values more than 10 K above the mean, with dashed lines and lighter shading indicating values more than 10 K below the mean (5-K interval). The corresponding lag days appear in the lower right contour of each panel.


Total PT Anomaly
High-frequency PT
Low-frequency PT
-8
-7
-6
-5
90N
75N
60N
45N
30N
120W
90W
60W
30W
0
30E
Latitude



2003), this issue is examined by adopting an initial value approach.

Given the finding of Limpasuvan and Hartmann (2000), that the high (low) NH annular mode index is associated with increased equatorward (poleward) wave activity, it is not surprising that the positive (negative) NAO events are characterized by anticyclonic (cyclonic) wave breaking. However, unlike their conclusion that monthly mean eddy fluxes play the major role for driving the NH annular mode, the evolution of daily synoptic patterns shown in this study illustrates the importance of submonthly time scale transient eddy fluxes. This discrepancy may be explained by the fact that their analysis was based on a flow partition into monthly mean and deviation from that mean. Because the time scale of the NAO life cycle is much shorter than one month, it is highly likely that the monthly mean eddy fluxes ultimately come from the fluxes of much shorter time scale transients.

The above consideration helps us to speculate on the question of why global warming may correspond to the NAO index being skewed toward the positive phase (Thompson et al. 2000). If a warmer climate drives a stronger and more poleward-intruding subtropical jet, then the probability of baroclinic waves encountering the equatorward side of this jet is expected to increase. As the horizontal shear on the equatorward side of the jet is anticyclonic, the probability of anticyclonic wave breaking will also increase. A systematic change in such a probability distribution will manifest into a NAO trend toward the positive phase. While this is a conjecture that needs to be tested, it underscores the importance of understanding the intrinsic time scale behavior of the NAO, even when the primary interest lies in assessing much longer time scale behavior.

Acknowledgments. We thank Christian Franzke and Seok-Woo Son for their useful discussions. We would also like to thank two anonymous reviewers for their helpful comments. Part of this study is based on the lead author's undergraduate honors thesis. This research was supported by the National Science Foundation through Grant ATM-0003039. We acknowledge the NOAA Climate Diagnostic Center for providing us with the NCEP–NCAR reanalysis dataset.

APPENDIX A

Projection Analysis

In order to interpret the NAO evolution described by Feldstein (2003), we perform the same analysis as in Feldstein (1998, 2002, 2003; see also Franzke et al.

←

FIG. 10. As in Fig. 9 except from lag −8 to lag −3 days for the negative NAO case depicted in Fig. 6.

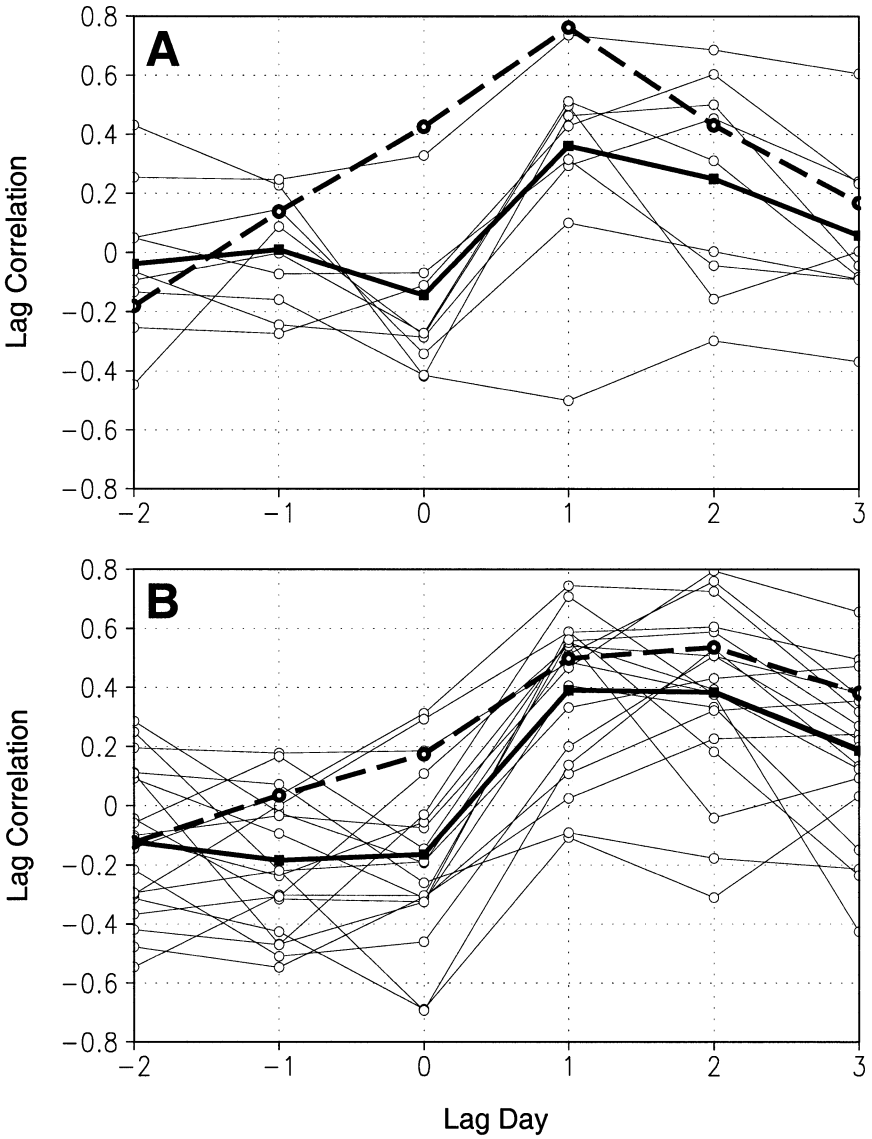


FIG. 11. Lag correlations between the time series of the projection of the high-frequency Θ field onto the total Θ anomaly field, and that of the low-frequency Θ filed onto the total Θ anomaly field for (a) positive-phase and (b) negative-phase events. Positive lag means the time series of the low-frequency projection lags that of the high-frequency projection. Thin solid lines denote individual-case lag correlations and thick solid lines represent the composite lag correlation. The lag correlation profiles for the NAO events examined in Figs. 2 and 6 (positive and negative phases, respectively) are indicated by thick dashed lines in (a) and (b), respectively. Against a zero-correlation null hypothesis, the 99.9% confidence level is 0.22. See the text for more details.

2001) but for individual NAO events rather than for composites.

Our analysis of the streamfunction tendency equation is based on Cai and Van den Dool (1994). Symbolically, the streamfunction tendency equation can be written as

$$\frac{\partial \psi^L}{\partial t} = \sum_{i=1}^{8} \xi_i, \tag{A1}$$

where the dominant terms on the right-hand side of (A1) correspond to planetary vorticity advection by the anomalies, relative vorticity advection that involves interaction of the anomalies with either the zonally symmetric or zonally asymmetric climatological flow, the divergence term, and driving by high- and low-frequency transient eddy vorticity fluxes. The eddies that comprise these fluxes are separated by a 10-day cutoff period. Equation (A1) is described in detail in appendix B. A brief description of the physical meaning of each term in (A1) is also presented in appendix B.

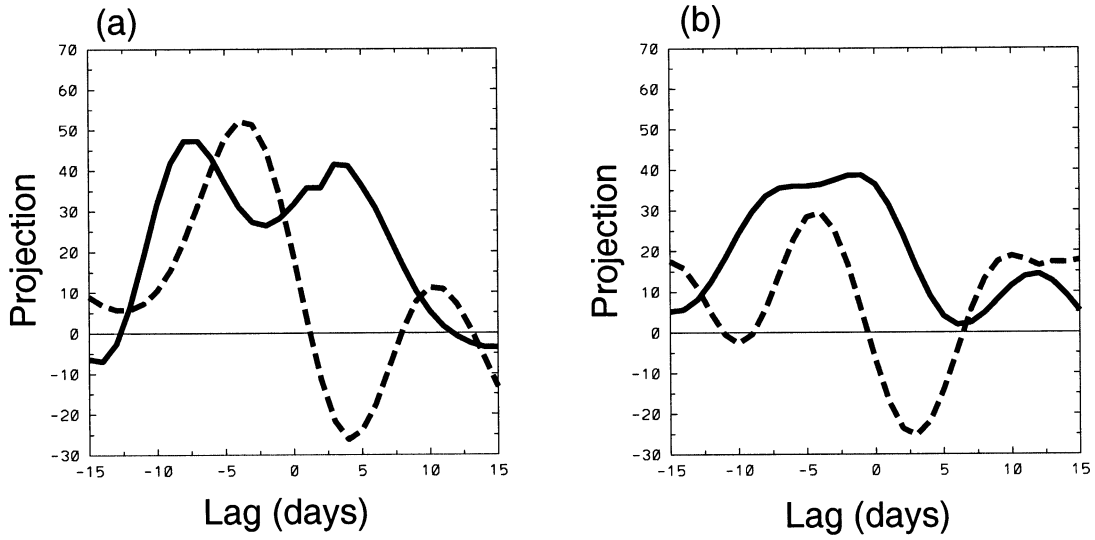


FIG. 12. The time-lagged projections by the high-frequency transient eddy vorticity fluxes (solid line) and low-frequency transient eddy vorticity fluxes (dashed line) for (a) the positive-phase example of Fig. 2 and (b) the negative-phase example of Fig. 6. See the text and appendixes A and B for more detail. The ordinate has been multiplied by $1.9 \times 10^7\ s^{-1}$ in (a) and $3.1 \times 10^7\ s^{-1}$ in (b).

We calculate projections of various terms on the rhs of (A1) onto the anomalous streamfunction field at the zero-lag day. As seen from the equations below, and as described in Feldstein (2003), this technique allows us to evaluate the role that each term on the rhs of (A1) plays toward the growth and decay of the NAO teleconnection pattern. Mathematically, this can be shown by first writing the projection P_i as

$$P_i = \sum_j \xi_{ij}(\lambda, \theta)\psi_{Mj}(\lambda, \theta)\cos\theta, \tag{A2}$$

where ξ_{ij} is the ith term on the rhs of (A1) and ψ_{Mj} is the anomalous streamfunction pattern for the zero-lag day, both variables being expressed at the jth gridpoint. The latitude and longitude are specified by the variables θ and λ, respectively. The summation in (A2) extends over all gridpoints within the Northern Hemisphere.

The meaning of these projections, as discussed in Feldstein (2003), can be seen by first specifying the anomalous streamfunction at time t to take the form

$$\psi(\lambda, \theta, t) = a(t)\psi_{Mj}(\lambda, \theta) + \psi'(\lambda, \theta, t). \tag{A3}$$

Writing $a(t)$ as

$$a(t) = \frac{\sum_j \psi(\lambda, \theta, t)\psi_{Mj}(\lambda, \theta)\cos\theta}{\sum_j \psi_{Mj}^2 \cos\theta} \tag{A4}$$

results in ψ_{Mj} being orthogonal to ψ'. Next, we substitute (A3) into (A1), multiply both sides of (A1) by $\psi_{Mj}\cos(\theta)$, and integrate over the entire Northern Hemisphere. Using the above orthogonality property yields

$$\frac{da}{dt} = \frac{\sum_{i=1}^{8} P_i}{\sum_j \psi_{Mj}^2 \cos\theta}. \tag{A5}$$

Thus, the expression in (A5) allows us to interpret the projections in (A2) as representing the influence of individual ξ_i on the rate of change with time of $a(t)$. Since the linear correlation between the composite $a(t)$ and NAO index exceeds 0.99 (Feldstein 2003), (A5) also enables us to determine quantitatively the extent to which each term on the rhs of (A1) contributes to the growth and decay of the NAO.

APPENDIX B

Streamfunction Tendency Equation

The individual terms in the streamfunction tendency equation are written as

$$\xi_1 = \nabla^{-2}\left[-(v_r^L + v_d^L)\frac{1}{a}\frac{df}{d\theta}\right]$$

$$\xi_2 = \nabla^{-2}(-[\overline{\mathbf{v}_r}]\cdot\nabla\zeta^L - \mathbf{v}_r^L\cdot\nabla[\overline{\zeta}]) + \nabla^{-2}(-[\overline{\mathbf{v}_d}]\cdot\nabla\zeta^L - \mathbf{v}_d^L\cdot\nabla[\overline{\zeta}])$$

$$\xi_3 = \nabla^{-2}(-\overline{\mathbf{v}_r^*}\cdot\nabla\zeta^L - \mathbf{v}_r^L\cdot\nabla\overline{\zeta^*}) + \nabla^{-2}(-\overline{\mathbf{v}_d^*}\cdot\nabla\zeta^L - \mathbf{v}_d^L\cdot\nabla\overline{\zeta^*})$$

$$\xi_4 = \nabla^{-2}[-(f+\overline{\zeta})\nabla\cdot\mathbf{v}_d^L - \zeta^L\nabla\cdot\overline{\mathbf{v}_d}]$$

$$\xi_5 = \nabla^{-2}(-\mathbf{v}_r^L\cdot\nabla\zeta^L)^L + \nabla^{-2}[-\nabla\cdot(\mathbf{v}_d^L\zeta^L)]^L$$

$$\xi_6 = \nabla^{-2}(-\mathbf{v}_r^H \cdot \boldsymbol{\nabla}\zeta^H)^L + \nabla^{-2}[-\boldsymbol{\nabla} \cdot (\mathbf{v}_d^H \zeta^H)]^L$$

$$\xi_7 = \nabla^{-2}(-\mathbf{v}_r^L \cdot \boldsymbol{\nabla}\zeta^H)^L + \nabla^{-2}[-\boldsymbol{\nabla} \cdot (\mathbf{v}_d^L \zeta^H)]^L + \nabla^{-2}(-\mathbf{v}_r^H \cdot \nabla\zeta^L)^L + \nabla^{-2}[-\boldsymbol{\nabla} \cdot (\mathbf{v}_d^H \zeta^L)]^L$$

$$\xi_8 = \nabla^{-2}\left[-\mathbf{k} \cdot \boldsymbol{\nabla} \times \left(w^L \frac{\partial \overline{\mathbf{v}}}{\partial p}\right)\right] + \nabla^{-2}\left[-\mathbf{k} \cdot \boldsymbol{\nabla} \times \left(\overline{w} \frac{\partial \mathbf{v}^L}{\partial p}\right)\right] + \nabla^{-2}\left[-\mathbf{k} \cdot \boldsymbol{\nabla} \times \left(\frac{w' \partial \mathbf{v}'}{\partial p}\right)\right]^L,$$

where ψ is the streamfunction, ζ the relative vorticity, $\mathbf{v}$ the horizontal wind vector, v the meridional wind component, ω the vertical wind component, a the earth's radius, f the Coriolis parameter, and θ is latitude. The subscripts r and d denote the rotational and divergent components of the horizontal wind, respectively; and the superscripts H and L indicate quantities that are 10-day high- and low-pass filtered, respectively. The time mean for the 1958–97 December to February period is subtracted from the low-pass-filtered quantities. The time mean is denoted by an overbar and the deviations from the time mean by a prime. Zonal averages are denoted by square brackets, and deviations from the zonal average by an asterisk.

Briefly, ξ_1 corresponds to planetary vorticity advection by the anomalies, ξ_2 (ξ_3) to relative vorticity advection involving the interaction of the anomalies with the zonally symmetric (asymmetric) climatological flow, ξ_4 to the divergence term, and ξ_5 (ξ_6) to driving by the interaction among low (high) frequency transient eddies. The quantities ξ_7 and ξ_8 represent driving due to the interaction between high- and low-frequency transient eddies and the tilting term, respectively.

REFERENCES

Berggren, R., B. Bolin, and C.-G. Rossby, 1949: An aerological study of zonal motion, its perturbations and break-down. *Tellus*, **1,** 14–37.

Cai, M., and H. M. Van den Dool, 1994: Dynamical decomposition of low-frequency tendencies. *J. Atmos. Sci.,* **51,** 2086–2100.

Cash, B., and S. Lee, 2001: Observed nonmodal growth of the Pacific–North American teleconnection pattern. *J. Climate,* **14,** 1017–1028.

Davis, C. A., and K. A. Emanuel, 1991: Potential vorticity diagnostics of cyclogenesis. *Mon. Wea. Rev.,* **119,** 1929–1953.

Feldstein, S. B., 1998: The growth and decay of low-frequency anomalies in a GCM. *J. Atmos. Sci.,* **55,** 415–428.

——, 2000: Teleconnections and ENSO: The timescale, power spectra, and climate noise properties. *J. Climate,* **13,** 4430–4440.

——, 2002: Fundamental mechanisms of PNA teleconnection pattern growth and decay. *Quart. J. Roy. Meteor. Soc.,* **128A,** 775–796.

——, 2003: The dynamics of NAO teleconnection pattern growth and decay. *Quart. J. Roy. Meteor. Soc.,* **129,** 901–924.

Franzke, C., K. Fraedrich, and F. Lunkeit, 2001: Teleconnections and low-frequency variability in idealized experiments with two storm tracks. *Quart. J. Roy. Meteor. Soc.,* **127,** 1321–1339.

——, S. Lee, and S. B. Feldstein, 2003: Is the North Atlantic Oscillation a breaking wave? *J. Atmos. Sci.,* **61,** 145–160.

Grotzner, A., M. Latif, and T. P. Barnett, 1998: A decadal climate cycle in the North Atlantic Ocean as simulated by the ECHO coupled GCM. *J. Climate,* **11,** 831–847.

Hoskins, B. J., and P. D. Sardeshmukh, 1987: A diagnostic study of the dynamics of the Northern Hemisphere winter of 1985–86. *Quart. J. Roy. Meteor. Soc.,* **113,** 759–778.

——, I. N. James, and G. H. White, 1983: The shape, propagation and mean-flow interaction of large-scale weather systems. *J. Atmos. Sci.,* **40,** 1595–1612.

Lee, S., and S. B. Feldstein, 1996: Two types of wave breaking in an aquaplanet GCM. *J. Atmos. Sci.,* **53,** 842–857.

Limpasuvan, V., and D. L. Hartmann, 2000: Wave-maintained annular modes of climate variability. *J. Climate,* **13,** 4414–4429.

Palmen, E., and C. W. Newton, 1969: *Atmospheric Circulation Systems.* Academic Press, 603 pp.

Rodwell, M. J., D. P. Rowell, and C. K. Folland, 1999: Oceanic forcing of the wintertime North Atlantic Oscillation and European climate. *Nature,* **398,** 320–323.

Shabbar, A., J. Huang, and K. Higuchi, 2001: The relationship between the wintertime North Atlantic Oscillation and blocking episodes in the North Atlantic. *Int. J. Climatol.,* **21,** 355–369.

Shindell, D. T., R. L. Miller, G. Schmidt, and L. Pandolfo, 1999: Simulation of recent northern winter climate trends by greenhouse-gas forcing. *Nature,* **399,** 452–455.

Shutts, G. J., 1983: The propagation of eddies in diffluent jetstreams: Eddy vorticity forcing of ''blocking'' flow fields. *Quart. J. Roy. Meteor. Soc.,* **109,** 737–761.

Simmons, A. J., and B. J. Hoskins, 1980: Barotropic influences on the growth and decay of nonlinear baroclinic waves. *J. Atmos. Sci.,* **37,** 1679–1684.

Swanson, K. L., P. J. Kushner, and I. M. Held, 1997: Dynamics of barotropic storm tracks. *J. Atmos. Sci.,* **54,** 791–810.

Thompson, D. W. J., and J. M. Wallace, 1998: The Arctic Oscillation signature in the wintertime geopotential height temperature fields. *Geophys. Res. Lett.,* **25,** 1297–1300.

——, and ——, 2000: Annular modes in the extratropical circulation. Part I: Month-to-month variability. *J. Climate,* **13,** 1000–1016.

——, ——, and G. C. Hegerl, 2000: Annular modes in the extratropical circulation. Part II: Trends. *J. Climate,* **13,** 1018–1036.

Thorncroft, C. D., B. J. Hoskins, and M. E. McIntyre, 1993: Two paradigms of baroclinic wave life-cycle behavior. *Quart. J. Roy. Meteor. Soc.,* **119,** 17–55.